A neural circuit for flexible control of persistent behavioral states

Ni Ji[1], Gurrein K. Madan[1], Guadalupe I. Fabre[1], Alyssa Dayan[1], Casey M. Baker[1], Ijeoma Nwabudike[1], Steven W. Flavell[1,2,3]

[1]Picower Institute for Learning & Memory, Department of Brain & Cognitive Sciences, Massachusetts Institute of Technology, Cambridge, MA 02139, USA

[2]Lead Contact

[3]Correspondence: flavell@mit.edu

Summary

To adapt to their environments, animals must generate behaviors that are closely tuned to a dynamically changing sensory world. However, behavioral states such as foraging or mating typically persist over long time scales to ensure proper execution. It remains unclear how neural circuits generate stable activity patterns to drive behavioral states, while maintaining the flexibility to select among alternative states when the sensory context changes. Here, we elucidate the functional architecture of a neural circuit controlling the choice between exploration and exploitation states during foraging in *C. elegans*. We identify stable circuit-wide activity patterns underlying each behavioral state and show that feedback between a sensorimotor circuit and two antagonistic neuromodulatory inputs underlies the emergence of these network states. Sensory processing neurons that detect salient food cues can couple to either neuromodulatory system and bias the network towards different states in different sensory contexts. This allows animals to dynamically adjust the balance between exploration and exploitation during foraging. Our results demonstrate that bi-directional communication between sensorimotor and neuromodulatory circuits allows animals to flexibly select behavioral states appropriate for their sensory context. This neural circuit motif may be broadly used in a variety of cases where animals need to balance behavioral persistence with sensitivity to environmental change.

Introduction

The behavioral state of an animal—whether it is active, inactive, feeding or sleeping—can profoundly influence its perception of and response to the environment (Anderson, 2016; Artiushin and Sehgal, 2017; Lee and Dan, 2012; Maimon, 2011; Nichols et al., 2017). In contrast to fast actions, behavioral states are often highly stable, lasting up to hours or days. Despite this remarkable stability, animals can flexibly choose their behavioral state based on sensory context and switch between states when the contextual milieu changes (Andalman et al., 2019; Clowney et al., 2015; Hoopfer et al., 2015). How behavioral states are controlled at the circuit level to achieve both stability and flexibility remains poorly understood.

At the neural level, long-lasting behavioral states often stem from persistent activity patterns within circuits. Long-standing theoretical work (Li et al., 2016; Major and Tank, 2004; Seung, 1996; Wang, 2012) and recent experimental evidence (Inagaki et al., 2019; Li et al., 2016) has highlighted the role of recurrent circuitry in driving persistent neural activity. From a theoretical perspective, functional circuits with mutual excitation, mutual inhibition, or both could generate multiple stable activity states (Goldman et al., 2007; Machens et al., 2005; Wang, 2001; Xiong and Ferrell Jr, 2003). While this circuit property favors the generation of stable states, it could also prevent the circuit from flexibly switching between alternative states in response to dynamically-varying inputs. Circuit architectures that allow for the generation and flexible control of alternative persistent circuit states remain to be identified.

In addition to recurrent circuit architecture, studies across model organisms have also suggested a critical role for neuromodulation in behavioral state control (Ache et al., 2019; Bargmann, 2012; Chew et al., 2018; Hoopfer et al., 2015; Marder, 2012; Rengarajan et al., 2019; Seo et al., 2019). Moreover, recent studies suggest that contextual cues must converge with neuromodulatory systems to impact behavioral state selection. For example, serotonergic neurons

in the dorsal raphe nucleus of the mouse suppress movement in low-threat environments, but facilitate movement in high-threat contexts (Seo et al., 2019). In flies, octopamine modulation can bias the dual outputs of male P1 interneurons to favor aggression over courtship (Hoopfer et al., 2015; Watanabe et al., 2017). Recent efforts have begun to map out anatomical inputs to brain neuromodulatory centers (Breton-Provencher and Sur, 2019; Schwarz and Luo, 2015; Weissbourd et al., 2014). However, the functional circuit architectures that link sensory context with neuromodulation and behavior remain poorly understood.

To understand how behavioral states are generated and controlled at the circuit level, we examined the neural circuit controlling the balance between exploration and exploitation during foraging in the nematode *C. elegans*. In the presence of bacterial food, *C. elegans* display two alternative behavioral states called dwelling and roaming, in which they display movement patterns that allow them to either exploit their current food source or explore for better resources, respectively (Figure 1A) (Arous et al., 2009; Flavell et al., 2013; Fujiwara et al., 2002; Shtonda and Avery, 2006). Each state lasts from minutes to hours, and transitions between states are abrupt (Flavell et al., 2013). Transitions between roaming and dwelling are influenced by many factors, including the animal's detection and ingestion of food, their satiety level, and other sensory cues (Arous et al., 2009; Gallagher et al., 2013). Food ingestion is detected by the serotonergic sensory neuron NSM (Rhoades et al., 2019) and food odors are detected by a group of chemosensory neurons (Arous et al., 2009; Fujiwara et al., 2002). Mechanical and aversive sensory inputs can also elevate roaming (Chew et al., 2018; Choi et al., 2013, 2015). We previously identified a central circuit that controls roaming and dwelling states. The neuromodulator 5-HT promotes dwelling, while pigment-dispersing factor (PDF) neuropeptides promote roaming (Choi et al., 2013; Flavell et al., 2013; Sawin et al., 2000). While genetic analyses have identified key neurons that make and

detect these neuromodulators (Flavell et al., 2013) (Figure 1B), the circuit-level mechanisms by which these persistent behavioral states are maintained and controlled remain unclear.

Here, we elucidate the functional architecture of the circuit that controls context-specific selection of roaming and dwelling foraging states in *C. elegans*. We identify stable circuit-wide activity patterns underlying each behavioral state and show that feedback between a sensorimotor circuit and two antagonistic neuromodulatory inputs underlies the emergence of these network states. Sensory processing neurons that detect salient food cues can couple to either neuromodulatory system and bias the network towards different states in different sensory contexts, allowing animals to dynamically adjust the balance between exploration and exploitation in complex foraging environments. These results indicate that bi-directional communication between sensorimotor and neuromodulatory circuits allows animals to flexibly select behavioral states appropriate for their sensory context.

Results

Stable, low-dimensional circuit states correspond to roaming and dwelling states

To characterize neural circuit dynamics during foraging, we built a calcium imaging platform with a closed-loop tracking system that allows for simultaneous calcium imaging of many *C. elegans* neurons in freely-moving animals (Figures 1A, S1A, and S1B; movement controls in Figure S2) (Faumont and Lockery, 2006; Nguyen et al., 2016; Venkatachalam et al., 2015). We generated a transgenic line where well-defined promoter fragments were used to express GCaMP6m in a select set of 10 neurons (Figures 1B and S1C). These neurons were selected to fall into three groups: 1) neurons known to release/detect 5-HT or PDF (Flavell et al., 2013), 2) neurons that share dense synaptic connections with those in 1), and 3) premotor or motor neurons whose

activities report the locomotory intent of animals (Li et al., 2014; Roberts et al., 2016). Calcium imaging of this defined subset of neurons allows us to leverage prior knowledge and easily determine the identity of each neuron in our recordings, thus circumventing the challenge of determining neuronal identity in a densely-labeled brain.

Because several of the recorded neurons are known to control locomotion, we first asked if the activity of each neuron was correlated with the direction or speed of locomotion. We found that nine of the recorded neurons were differentially active depending on the direction of locomotion (Figure 1C and 1D). For example, the AVB, AIY, and RIB neurons exhibited higher activity during forward locomotion, while the AVA neuron was more active when animals reversed direction to turn (reversals). These observations are consistent with the known roles of these neurons in locomotion (Li et al., 2014; Roberts et al., 2016; Tsalik and Hobert, 2003). We also asked whether the recorded neurons differed in their activities over longer time scales, during roaming versus dwelling states. Six of the recorded neurons showed differential activity between roaming and dwelling states (Figure 1C and 1D). The serotonergic neuron NSM exhibited higher activity during dwelling, while most of the forward- and reversal-selective neurons were more active during roaming. Thus, neural activity in this circuit is associated with acute locomotion parameters and foraging states.

To identify the dominant modes of dynamics in this circuit, we performed Principal Component Analysis (PCA) using the activity profiles of all the recorded neurons. The top two principal components (PC1 and PC2, which explained 29% and 15% of the total variance, respectively) exhibited clear behavioral correlates. Consistent with previous work (Kato et al., 2015), neural activity during forward and reverse locomotion segregated along PC1. In addition, we found that the roaming and dwelling states corresponded to low and high values on PC2 (Figure

1E). This robust mapping between circuit activity and behavior implicates stable circuit activity states as the underlying basis for persistent behavioral states.

Although multiple neurons exhibited different activity profiles during roaming compared to dwelling, only NSM's activity served as a direct correlate of a behavioral state. High levels of NSM activity reliably coincided with periods of dwelling and high PC2 values (Figure 1F) and were associated with a robust cessation of high velocity locomotion (Figure 1G). Our data also suggested that the onset of NSM activation coincided with stereotyped changes in circuit dynamics: NSM activation onset frequently occurred during a period of high activity on PC1 and low activity on PC2, typical of forward locomotion during roaming (Figure 1H and 1I). As NSM became active, circuit activity rose rapidly along PC2. After reaching a peak on PC2, circuit activity slowly traveled towards low values of both PC1 and PC2, hitting a corner of the PC space corresponding to the animal in reverse locomotion (Figure 1H and 1I). Optogenetic activation of NSM in roaming animals evoked a similar trajectory in circuit activity, albeit with subtle differences (Figure S3A). These results suggest that roaming-to-dwelling transitions are associated with a reliable change in circuit dynamics.

The serotonergic NSM neuron sustains its own activity via mutual inhibition with its target neurons

To elucidate the functional architecture of this circuit, we next sought to understand how neuromodulator release impacts circuit dynamics. Previous work has established important roles for 5-HT and PDF signaling in the control of roaming and dwelling behaviors (Choi et al., 2013; Flavell et al., 2013; Rhoades et al., 2019; Sawin et al., 2000), but their impact on circuit dynamics

is not known. To address this, we recorded circuit activity in mutants that are deficient in 5-HT signaling, PDF signaling, or both (Figures 2 and 3).

In each mutant, we examined the activities of individual neurons and coordination between the neurons. Wild-type animals exhibited mutual exclusivity in the activities of the serotonergic NSM neuron and the PDF-1-producing AVB neuron (Figures 2C and S3B). This pattern mirrors the behavior-level antagonism between roaming and dwelling states. As was previously shown, mutants deficient in 5-HT synthesis (*tph-1*) displayed a significant reduction in time spent dwelling (Figure 2E). The mutual exclusivity between NSM and AVB remained intact in these animals (Figure 2A and 2D), but the average duration of NSM activation was dramatically shortened (Figure 2F). This suggests that 5-HT signaling is required to maintain NSM activity. Such a result could be explained by an excitatory 5-HT receptor on NSM or a circuit-level effect. To test for circuit-level effects, we examined mutants deficient in the inhibitory 5-HT receptor MOD-1, which is expressed on several target neurons and is known to be critical for long-lasting dwelling (Flavell et al., 2013). The *mod-1* mutants also displayed dramatically shortened NSM-on states, suggesting that the downstream *mod-1*-expressing neurons, whose activities are suppressed by 5-HT signaling, play a functional role in inhibiting NSM (Figure 2B and 2D). Thus, the serotonergic NSM neuron reinforces its own activity via mutual inhibition with the 5-HT target neurons expressing MOD-1 (Figure 2G). The 5-HT target neurons that express MOD-1, such as AIY, RIF, ASI, and RID, do not form synapses onto NSM, suggesting that they must functionally inhibit NSM through a polysynaptic route or via a diffuse neuromodulator.

PDF target neurons inhibit the serotonergic NSM neuron to maintain exclusivity of the opposing circuit states

We next examined the impact of PDF signaling on circuit dynamics by imaging animals carrying a null mutation in the PDF receptor gene *pdfr-1* (Figure 3A). The mutual exclusivity between NSM and AVB was strongly disrupted in these animals (Figure 3C and S3B). The two neurons were coactive 20% of the time in *pdfr-1* mutants, compared to 5% in wild type (Figures 2C and 3C). During periods of NSM-AVB coactivity, other forward-promoting neurons were also co-active and the animal moved forward at speeds mid-way between those typically seen for roaming and dwelling in wild type (Figure 3D shows speed distributions). This suggests that co-activation of the 5-HT and PDF neurons may send competing commands to the downstream motor circuit, which could blur the boundary between roaming and dwelling states. NSM activation bouts were also longer in *pdfr-1* mutants, as compared to wild type (Figure 3E). This observation, together with the ectopic co-activity of NSM and AVB, suggests that PDF signaling during roaming acts through PDFR-1 target neurons to suppress NSM activity. Consistent with this interpretation, constitutive activation of PDFR-1 signaling, via cell-specific expression of the hyperactive PDFR-1 effector ACY-1(P260S), strongly inhibited NSM activity (Figures 3B-C and S3B). Together, these results suggest that PDF signaling is required to keep NSM inactive during roaming states, a key requirement for the exclusivity of these alternative behavioral states.

Serotonin and PDF target neurons contribute to the same mutual inhibitory circuit

To probe whether the 5-HT and PDF target neurons act in the same pathway to suppress NSM activity, we performed epistasis analysis by examining *tph-1;pdfr-1* double mutants. Similar to *pdfr-1* mutants, these animals exhibited ectopic co-activity of NSM and AVB and long bouts of NSM activation, suggesting that *pdfr-1* functions downstream of *tph-1* to control NSM activity (Figures 3C, 3E and S3B). Consistent with this result, we found that optogenetic activation of the

mod-1-expressing 5-HT target neurons, which triggers roaming in wild-type animals, failed to do so in *pdfr-1* mutants (Fig. 3F). Thus, the PDF target neurons likely act downstream of the 5-HT target neurons to inhibit NSM activity (Fig. 3G). Because NSM does not express *pdfr-1* (Rhoades et al., 2019; Spencer et al., 2014) and does not receive direct synaptic input from the other neurons studied here, it is likely that the feedback signal is a neuromodulator that is not yet identified.

Taken together, these data suggest that mutual inhibition between NSM and the downstream neurons targeted by 5-HT and PDF contributes critically to the stability and exclusivity of the circuit states that correspond to roaming and dwelling. In the *C. elegans* wiring diagram (White et al., 1986), several of the 5-HT and PDF target neurons receive dense synaptic inputs from chemosensory neurons and form synapses onto AVB and other downstream premotor neurons (Figure 3G). Thus, the 5-HT and PDF target neurons comprise a sensorimotor circuit that is bi-directionally connected to the neuromodulator-producing neurons NSM and AVB.

Stereotyped activity across the sensorimotor circuit precedes state transitions

We next sought to uncover how incoming chemosensory inputs might affect the balance between roaming and dwelling states. Based on the functional architecture described above, we hypothesized that activity changes in neurons in the sensorimotor circuit might precede and drive state transitions in wild-type animals. To test this hypothesis, we attempted to predict behavioral state transitions from circuit dynamics at preceding time points. Here, we focused on roaming-to-dwelling transitions since the neural correlate of this transition, NSM activation, was extremely reliable (Figure 1E and 1G). We trained a convolutional neural network (CNN) classifier to predict NSM activation using the multi-dimensional activity profile from all other neurons imaged (Figure 4A and B; see STAR Methods). The trained classifier reached ~75% test accuracy and revealed a

reliable activity pattern that preceded NSM activation (Figures 4C and S4A). This pattern indicates that NSM activation is likely to occur following heightened activity of the sensory processing neuron AIA and reduced activity of the roaming-active neurons, RIB and AVA (Figure 4C). Feature selection (see STAR Methods) revealed that the activity profile of AIA contributed critically to classifier performance (Figures 4C and S4B). This result prompted us to investigate the role of AIA in the roaming-dwelling behaviors.

The vast majority of AIA's synaptic inputs (~80%) are from chemosensory neurons (Figure S4C), several of which have been reported to detect temporal changes in the concentrations of olfactory and gustatory cues (Chalasani et al., 2007; Larsch et al., 2015; Suzuki et al., 2008). Previous work has shown that AIA generates robust neural responses to the acute delivery of attractive odorants present in bacterial food and to bacteria-conditioned media (Dobosiewicz et al., 2019; Larsch et al., 2015). Consistent with these sensory responses, AIA is critical for chemotaxis towards food odors in non-feeding animals. AIA sends synaptic output to other neurons in the sensorimotor pathway. Silencing experiments have shown that AIA activity is required to extend forward runs while the concentration of food odors increases (Larsch et al., 2015).

During roaming, AIA activity was selectively active during forward movement but not during reversals. Thus, AIA was positively correlated with neurons active during forward runs, such as AIY and RIB, during the roaming state (Figures 5A shows correlations between the neurons before, during, and after state transitions). This activity profile is consistent with AIA's role in driving forward runs during chemotaxis. This positive coupling, however, began to attenuate prior to NSM activation (Figure 5A, S5A and S5B). At this time, the average activity of AIA began to rise while that of the roaming-active neurons remained at similar levels (Figure 5B and 5C; also see examples in Figure 4A). At the onset of dwelling states, AIA stayed co-active

with NSM for up to several minutes, leading to a period of positive coupling between the two neurons while the roaming-active neurons displayed reduced activity (Figures 5D-F and S5C; also see examples in Figure 4A). Thus, in feeding animals, AIA activity can switch from co-varying with the forward-active neurons during roaming to positively coupling with NSM during dwelling.

The sensory processing neuron AIA acts upstream of the neuromodulatory systems to control state switching

Because AIA exhibited functional coupling with both roaming-active and dwelling-active neurons, we next tested whether AIA activation can elicit behaviors typical of either state. We optogenetically activated AIA in foraging animals and found that this activation led to different responses depending on the animal's behavior at the moment of stimulation. AIA activation triggered an acute reduction in speed in over half of the roaming animals and led to a gradual increase in speed in dwelling animals (Figures 5G and S5D). To test whether AIA acts through 5-HT and PDF to drive these behaviors, we optogenetically activated AIA in 5-HT- or PDF-null mutants (*tph-1* and *pdfr-1*, respectively). In *tph-1* mutants, the slowing of the roaming animals was no longer significant compared to control animals, while the speeding of the dwelling animals remained significant (Figures 5H and S5D). Consistent with this finding, stimulating AIA in roaming animals triggered transient NSM activation coincident with slowing (Figure S5E). Conversely, in *pdfr-1* mutants, the speeding effect was abolished (Figure 5I and S5D; *pdfr-1* animals did not roam frequently enough to examine the slowing effect). Thus, AIA can drive dwelling-like behaviors by activating the 5-HT system and, at other times, can drive roaming-like behaviors via activation of the PDF system (Figure 5J).

AIA couples the sensory context to the selection of roaming versus dwelling states

Because AIA receives abundant sensory inputs and has apparent bidirectional outputs, we hypothesized that AIA may promote either roaming or dwelling depending on salient cues in the environment. To test this hypothesis, we compared the behavior of wild-type animals to those in which AIA had been silenced (*AIA::unc-103gf*). We exposed these animals to two different foraging environments: (1) a patch foraging assay where animals on a sparse food patch can navigate a food odor gradient to move towards an adjacent dense food patch (Figure 6A); and (2) a food exposure assay where animals are directly exposed to different densities of uniformly-seeded food (Figure 6J). In the first context, the odor gradient emanating from the dense food patch could allow animals to explore towards a better food source. In the second context, an unchanging odor environment and the availability of food may prompt animals to exploit the local food source.

In the patch foraging assay, wild-type animals exhibited directed motion towards the dense food patch and alternated between roaming and dwelling as they approached (Figure 6A, bottom). Animals exhibited several behavioral strategies that facilitated movement along the gradient direction towards the dense food patch (i.e. positive chemotaxis). First, animals on the sparse food side of the plates exhibited higher levels of roaming than control animals situated on identical sparse food lawns without any dense food nearby (Figure 6B). In addition, animals displayed directed movement towards the dense food lawn (i.e. positive chemotaxis) predominantly while they were roaming (Figure 6C and 6D). Secondly, roaming animals preferentially transitioned into dwelling states when their chemotactic performance dropped (Figure 6E). A related phenomenon was that the instantaneous speed of the animals co-varied with their direction of locomotion, lagging by a few seconds (Figure 6F). Mutants defective in chemosensation (*tax-4*) (Komatsu et al., 1996) did not display any of the above navigational strategies and failed to navigate to the

dense food patch (Figures 6G-I, and S6A). These results indicate that the food odor gradient can drive an overall increase in roaming and control the transitions between roaming and dwelling.

We next asked whether AIA plays a role in regulating the roaming and dwelling states during navigation to dense food. AIA-silenced animals (*AIA::unc-103gf*) were defective in all navigational strategies: they failed to elevate roaming, displayed reduced positive chemotaxis, and did not couple the roaming-to-dwelling transition with chemotactic performance (Figures 6G-I and S6A). These results confirm a critical role for AIA in regulating roaming and dwelling in dynamic sensory environments, and suggest that AIA promotes the roaming state during navigation of the odor gradient.

We also examined mutants defective in either PDF or 5-HT signaling. *pdfr-1* mutants display reduced roaming in the food odor gradient (Figure 6G). However, they continued to exhibit positive chemotaxis during roaming and initiated dwelling when their chemotactic performance began to drop (Figures 6H, 6I, and S6A). *tph-1* mutants displayed enhanced roaming and did not switch to dwelling when their chemotactic performance dropped (Figures 6G, S6A and S6B). Thus, AIA and the neuromodulatory systems are required for adaptive roaming/dwelling regulation in a food odor gradient. Consistent with an important role for AIA in relaying sensory information to the roaming-dwelling circuit, we also found that direct optogenetic activation of AWA olfactory neurons, which detect increases in food odors, evoked roaming-like behavior in an AIA-dependent manner (Figure S6C). This result provides additional evidence that AIA promotes roaming in response to the detection of increased food odors.

Finally, we examined animals in the second sensory context, where they were directly placed on plates with different densities of uniformly-seeded food (Figures 6J). Consistent with previous studies (Arous et al., 2009), we found that wild-type animals increased their time spent

dwelling on denser bacterial food sources, primarily by extending their dwelling state durations (Figures 6J-K and S6D). AIA-silenced animals displayed a decrease in their dwelling state durations in this sensory context compared to wild-type animals, most notably in the high-density food environment (Figures 6K). Thus, AIA functions to promote dwelling when animals are directly exposed to a uniformly-seeded food resource. Together with the above data, these results suggest that AIA plays a critical role in modulating roaming and dwelling states depending on the sensory context, and can promote different behavioral states in different contexts.

Discussion

Our findings show that a sensorimotor circuit and its neuromodulatory inputs reciprocally interact to enable flexible control of persistent behavioral states. In the roaming-dwelling circuit, these reciprocal interactions serve at least two important functions. First, mutual inhibition between the serotonergic NSM neuron and the PDF target neurons confers winner-take-all dynamics, which promotes the stability and mutual exclusivity of two opposing network states. This finding resonates with theoretical work on the role of mutual inhibition in brain dynamics (Romo et al., 2005; Wang, 2002). Secondly, outputs from the sensorimotor pathway onto both NSM and the PDF target neurons bring neuromodulation under direct sensory control and allows the sensory context to impact the balance between the roaming and dwelling states. Overall, this circuit architecture enables *C. elegans* animals to exhibit persistent roaming and dwelling states, while flexibly switching between them depending on the sensory context.

One notable aspect of the circuit architecture uncovered in this study (Figure 6L) is that the sensory processing neuron AIA, which detects appetitive food odors (Dobosiewicz et al., 2019; Larsch et al., 2015), provides dual outputs to both the dwelling-active NSM neuron and the

roaming-active neurons in the sensorimotor pathway (Figure 6L). This interpretation is supported by native AIA activity patterns that span both behavioral states, AIA's ability to drive behaviors typical of both states, and opposing effects of AIA silencing that depend on sensory context. Similar functional architectures, where a common input drives competing circuit modules, have been suggested to underlie behavior selection in other nervous systems (Anderson, 2016; Jovanic et al., 2016; Seo et al., 2019). One possible function of this motif in the roaming-dwelling circuit is that it could allow both the roaming- and dwelling-active neurons to be latently activated when the animal is exposed to food odors detected by AIA. In the presence of strong sensory input, such as an odor gradient, AIA outputs may drive roaming more strongly than dwelling (Figure S7A). This asymmetry could be amplified through mutual inhibition to bias the circuit towards the roaming state. When the animal migrates orthogonal to an odor gradient or is situated in a uniform food environment, the dynamic olfactory drive onto the roaming circuit is likely lowered. Under this condition, NSM, which is directly excited by food ingestion (Rhoades et al, 2019), may dominate the mutual inhibitory circuit to drive dwelling states (Figure S7B). Increased levels of food ingestion on denser food patches may further bias the output of the circuit towards the dwelling state, in a manner that is reinforced by AIA (Figure S7C and S7D). Thus, AIA activity may signal a general need to respond to food cues in the environment (i.e. roam or dwell) and, together with other inputs to the circuit, may specify the relative balance between the roaming and dwelling states.

Our data suggest that *C. elegans* can regulate its exploration and exploitation foraging states in different ways, depending on the context. In a uniform sensory environment, animals spontaneously transition between roaming and dwelling (Flavell et al., 2013). This is consistent with notions from Optimal Foraging Theory that both exploration and exploitation are needed to

maximum long-term energy gain (Bartumeus and Catalan, 2009). In this study, we show that the transitions between roaming and dwelling can also be dynamically modulated by odor gradients in the environment. We found that the 5-HT and PDF neuromodulatory systems that regulate stochastic state switching in uniform environments (Flavell et al., 2013) also control sensory-driven state changes (Fig. 6). The ability of this circuit to operate in these different modes is likely to be a consequence of its architecture, in which there is a winner-take-all mutual inhibitory loop that undergoes flip-flop transitions, but also incorporates incoming sensory inputs. Beyond foraging, exploration-exploitation tradeoffs are also relevant to cellular migration (Tan et al., 2013; Vergassola et al., 2007), as well as human (Cohen et al., 2007) and artificial intelligence (Sutton and Barto, 2018). It is possible that the algorithms and circuits that allow for flexible regulation of exploration-exploitation states may generalize across these diverse fields.

How do animals flexibly select among alternative behavioral states in a dynamically changing world? The complexity of the sensory world suggests that an exhaustive mapping from sensory contexts to behavioral outputs is implausible. Furthermore, a constantly changing environment may favor a “bet-hedging” strategy (Beaumont et al., 2009; Brockmann, 1987; Kussell and Leibler, 2005), where animals always favor some degree of behavioral state switching to buffer against unexpected conditions in the environment (e.g. an attractive odor gradient may not guarantee the presence of better food). The neural circuit identified in this study has several features that make it suitable to control behavioral states in this highly flexible manner. First, feedback between the sensorimotor pathway and its neuromodulatory inputs creates a mutual inhibitory loop that allows for the emergence of multiple stable behavioral states. Stochastic state switching could be driven by small fluctuations in either the external input to or the internal components of the circuit (Acar et al., 2008; Thiele et al., 2016). Secondly, common sensory drive

from AIA neurons that detect food odors latently activates competing circuit states and can facilitate either state when an animal is engaged in foraging for food. Lastly, context-specific sensory cues can provide additional drive onto either side of the winner-take-all circuit to bias the balance between states. This combination of mechanisms within the roaming-dwelling circuit may allow animals to adaptively select appropriate foraging states as they navigate a complex and ever-changing environment.

STAR METHODS

KEY REOURCES TABLE

Genotype	**Source**	**Identifier**
Wild-type Bristol N2	N/A	N2
flvEx46[[tph-1::GCaMP6m, mod-1::GCaMP6m, sto-3::GCaMP6m, glr-3::GCaMP6m, odr-2b::GCaMP6m, gcy-28.d::GCaMP6m, lgc-55(short)::GCaMP6m, nmr-1::GCaMP6m, tph-1::wrmScarlett, mod-1::wrmScarlett, nmr-1::wrmScarlett, sto-3::wrmScarlett]; lite-1(ce314), gur-3(ok2245)]	This study	SWF90
flvIs1[tph-1::GCaMP6m, mod-1::GCaMP6m, sto-3::GCaMP6m, glr-3::GCaMP6m, odr-2b::GCaMP6m, gcy-28.d::GCaMP6m, lgc-55(short)::GCaMP6m, nmr-1::GCaMP6m, tph-1::wrmScarlett, mod-1::wrmScarlett, nmr-1::wrmScarlett, sto-3::wrmScarlett]; lite-1(ce314), gur-3(ok2245)	This study	SWF113
flvIs1; lite-1(ce314); gur-3 (ok2245); mod-1(ok103)	This study	SWF186
flvIs1; lite-1(ce314); gur-3 (ok2245); pdfr-1(ok3425)	This study	SWF124
flvIs1; lite-1(ce314); gur-3 (ok2245); flvEx129[pdfr-1::acy-1gf, elt-2::nGFP]	This study	SWF263
flvEx46; lite-1(ce314); gur-3 (ok2245); tph1(mg280); pdfr-1(ok3425)	This study	SWF125
flvIs1; lite-1(ce314); gur-3 (ok2245); flvEx103[tph-1(short)::chrimson, elt-2::nGFP]	This study	SWF197
kyIs580[mod-1::nCre, myo-2::mCherry]; kyEx4816[ttx-3::ChR2(C128S)-GFP, odr-2b::inv[ChR2-sl2-GFP], myo-3::mCherry]	This study	CX14686
pdfr-1(ok3425); kyIs580[mod-1::nCre, myo-2::mCherry]; kyEx4816[ttx-3::ChR2(C128S)-GFP, odr-2b::inv[ChR2-sl2-GFP], myo-3::mCherry]	This study	CX14684
flvIs1; lite-1(ce314); gur-3 (ok2245); flvEx98[gcy-28.d::Chrimson, elt-2::nGFP]	This study	SWF194
flvIs1; lite-1(ce314); gur-3 (ok2245);tph-1(mg280); flvEx98[gcy-28.d::Chrimson, elt-2::nGFP]	This study	SWF216
flvIs1; lite-1(ce314); gur-3 (ok2245); pdfr-1(ok3425); flvEx98[gcy-28.d::Chrimson, elt-2::nGFP]	This study	SWF326
kyEx4745[gcy-28.d::unc-103gf::sl2-mCherry, elt-2::mCherry]	Larsch et al., 2015	CX14597
tax-4(p678) [5x backcrossed to N2]	This study	CX13078
pdfr-1(ok3425)	Flavell et al., 2013	CX14295
tph-1(mg280)	CGC	MT15434

flvEx54[gpa-6::CoChR, myo-3::mCherry]	This study	SWF103
flvEx54[gpa-6::CoChR, myo-3::mCherry]; kyEx4745[gcy-28.d::unc-103(gf)::sl2-mCherry, elt-2::mCherry]	This study	SWF315

CONTACT FOR REAGENT AND RESOURCE SHARING

Further information and requests for resources and reagents should be directed to and will be fulfilled by Lead Contact, Steven W. Flavell (flavell@mit.edu).

METHOD DETAIL

Growth conditions and handling

Nematode culture was conducted using standard methods (Brenner, 1974). Populations were maintained on NGM agar plates with *E. coli* OP50 bacteria. Wild-type was *C. elegans* Bristol strain N2. For genetic crosses, all genotypes were confirmed using PCR. Transgenic animals were generated by injecting DNA clones plus fluorescent co-injection marker into gonads of young adult hermaphrodites. One day old hermaphrodites were used for all assays. All assays were conducted at room temperature (~22°C).

Construction and characterization of multi-neuron GCaMP strain

To generate a transgenic strain expressing GCaMP6m in a specific subset of neurons involved in roaming and dwelling, we first generated pilot strains where one or two plasmids were injected at a time to optimized DNA concentrations. This also allowed us to determine the precise GCaMP6m and/or Scarlett expression pattern from each promoter. We then injected these plasmids as a mixture into *lite-1;gur-3* double mutants, which are resistant to blue light delivered during calcium imaging. We selected a line for use that had normal behavioral parameters and

showed relatively balanced expression of GCaMP6m and Scarlett in the target cells (SWF90). To obtain more consistent expression, the transgene was integrated by UV to generate *flvIs1* (SWF113). The integrated strain was outcrossed 4 times.

Microscope Design and Assembly

Overview. The tracking microscope design was inspired and based off previously described systems(Faumont and Lockery, 2006; Venkatachalam et al., 2015), with several modifications aimed at reducing motion artifacts and extending the duration of calcium imaging, so that long-lasting behavioral states could be examined. As illustrated in Figure S1, two separate light paths, below and above the specimen, were built onto a Ti-E inverted microscope (Nikon).

High-magnification light path for GCaMP imaging. The light path used to image GCaMP6m and Scarlett at single cell resolution is an Andor spinning disk confocal system. Light supplied from a 150mW 488nm laser and a 50mW 560nm laser passes through a 5000rpm Yokogawa CSU-X1 spinning disk unit with a Borealis upgrade (with a dual-camera configuration). A 40x/1.15NA CFI Apo LWD Lambda water immersion objective (Nikon) with a P-726 PIFOC objective piezo (PI) was used to image the volume of the worm's head. A custom quad dichroic mirror directed light emitted from the specimen to two separate Andor Zyla 4.2 USB3 cameras, which had in-line emission filters (525/50, and 625/90). Data was collected at 2x2 binning in a 512x512 region of interest in the center of the field of view.

Low-magnification light path for closed-loop tracking. A second light path positioned above the animal collected data for closed-loop tracking. Light supplied from a Sola SE2 365 Light Engine (Lumencor) passed through a DSRed (49005, Chroma) filter set and a 10x/0.3NA air

objective to excite Scarlett in the head of the worm. Red light emitted from the specimen passed through the filter set to an acA2000-340km Basler CMOS camera. Data was collected at 100 Hz.

Synchronized control of camera exposures and illumination light sources. The Andor Zyla cameras used for calcium imaging were run in rolling shutter mode. A trigger signal was generated by one of the two cameras whenever the camera shutter is fully open (~2 ms per exposure). This trigger signal served as a master control that synchronized several devices (Figure S1B). First, it was used to drive the 488nm and 560nm lasers, such that illumination is only provided when the full field of view is open. Second, the same trigger signal was used controlled the movement of the objective piezo, such that fast piezo movement occurs largely outside the window of laser illumination. Lastly, this signal was used to time the green LED used by the closed-loop tracking system. The LED was turned on only when the calcium imaging cameras were not actively acquiring images (i.e. outside the window when the rolling shutter is fully open) and when the lasers were off. Together, these approaches minimize photo-bleaching, photo-toxicity, and motion artifacts induced by movable parts of the microscope.

Closed-loop tracking software. A custom C/C++ software was used to process incoming frames from the tracking camera and to instruct the movement of a motorized stage (96S107-N3-LE2, Ludl; with a MAC6000 controller) to keep the head region of the animal at the center in the field of view. This software was adapted from Nguyen et al. with two key modifications: First, at each control cycle, the future velocity of the stage was calculated to match the predicted future velocity of the animal (i.e. predictive control as opposed to proportional control employed in previous study). Specifically,

$$v_{stage}(t + \Delta t) = v_{animal}(t) + \frac{(v_{animal}(t) - v_{animal}(t-1))}{\Delta t}$$

where $v_{stage}(t)$ is the instantaneous velocity of the stage and $v_{animal}(t)$ the instantaneous velocity of the animal. The latter was estimated as described below (see **Estimation of instantaneous animal location and velocity**). The right side of the formula was found empirically to be sufficient for predicting future animal velocity. The second modification was that we used the motion of the head region of the animal to extrapolate the locomotory state of the animal. This approach was empirically justified in a recent study and circumvents the need for a third light path for imaging the full body of the animal.

Behavioral Assays

Patch foraging assay. For the patch foraging assays, we used 24.5cm x 24.5cm NGM plates. Plates were uniformly seeded with sparse OP50 bacteria (OD 0.5 diluted 300x), and one half of the plate was seeded with dense bacteria (OD 0.5 concentrated 20x). The border between the sparse and dense food was always sharp and typically very straight. Plates were left overnight at room temperature. The following day, one-day old adult animals were picked to the sparse side of the food plate, approximately 1.5 cm from the dense food patch. Video recordings were started immediately, though for all analyses the first 20 min of data (equilibration time) was not analyzed. Videos were recorded at 3 fps using Streampix 7.0, a JAI SP-20000M-USB3 CMOS camera (41mm, 5120x3840, Mono) and a Nikon Micro-NIKKOR 55mm f/2.8 lens. Backlighting was achieved using a white panel LED (Metaphase Technologies Inc. White Metastandard 10” X 25”, 24VDC). Assay plates were placed on glass 3” above LEDs to avoid heat transfer to plates. Videos were processed using custom Matlab scripts, which included a step to manually confirm the exact frame of lawn encounter for each animal. Segmentation of behavior into roaming and dwelling was conducted as previously described (Flavell et al., 2013).

Foraging at different food densities. To examine animal behavior in uniform environments with different food densities, we seeded NGM plates (either circular 10 cm or 24.5x24.5cm) with different densities of food. For the experiments in Fig. 6, low-density was OP50 bacteria at OD 0.5 diluted 300x; high-density was OD 0.5 concentrated 20X. Plates grew overnight at room temperature. The following day, one day-old adult animals were picked to these plates and allowed to equilibrate for 45 mins, after which video recordings began. Videos were recorded and analyzed as described above.

Optogenetic stimulation during foraging behavior. For optogenetic stimulation of free-behaving animals, we picked one day-old adult animals to NGM plates seeded with 300X diluted OD 0.5 OP50 (supplemented with 50 uM all-trans-retinal) the night before. Animals were permitted to equilibrate for 45 min, after which videos were recorded using the setup described above. In these videos, light for optogenetic stimulation was delivered using a 625nm Mightex BioLED at 30 uW/mm^2. Patterned light illumination was achieved using custom Matlab scripts, which were coupled to a DAQ board (USB-6001, National Instruments) and BioLED Light Source Control Module (Mightex). Videos were analyzed as described above.

Data Analysis for Calcium Imaging

Semi-automated image segmentation to obtain neuron outlines. All image analyses were performed on maximum intensity projections of the collected z-stacks, since the neurons were well separated along the x-y axes. First, feature points and feature point descriptors were extracted for each frame of the calcium imaging video. Next, an N-by-N similarity matrix (N = number of frames in a video) was generated where each entry equals the number of matched feature points between a pair of frames. The columns of matrix were clustered using hierarchical clustering. Around 30 frames (typically 1-2% of frames from a video) were chosen across the

largest 15 clusters. These frames were then segmented manually. The user was asked to outline the region for interest (ROI) around each neuronal structure of interest (axonal segment for the AIY neurons, soma for all other neurons). After manual segmentation, the automatic segmentation software loops through each of the remaining frames. For each unsegmented frame (target frame), a best match (reference frame) was found among the segmented frames based on the similarity matrix. Then, geometrical transformation matrices were estimated using the locations of the matched feature points. The estimated transformation was then applied to the boundary vertices of each ROI in the reference frame to yield the estimated boundary of the same region in the target frame. Once done, the target frames with its automatically computed ROIs was included into the pool of segmented frames and could serve as a reference frame for the remaining unsegmented frames. This procedure was repeated iteratively through the rest of the video.

Estimation of instantaneous animal location and velocity. The instantaneous location of the animal $\begin{bmatrix} x_a \\ y_a \end{bmatrix}$ was calculated based on the following formula:

$$\begin{bmatrix} x_a \\ y_a \end{bmatrix} = \begin{bmatrix} x_s \\ y_s \end{bmatrix} + r * \begin{bmatrix} cos\theta & -sin\theta \\ sin\theta & cos\theta \end{bmatrix} \cdot \begin{bmatrix} x_c \\ y_c \end{bmatrix}$$

where $\begin{bmatrix} x_s \\ y_s \end{bmatrix}$ is the instantaneous location of the microscope stage, $\begin{bmatrix} x_c \\ y_c \end{bmatrix}$ is the position of the head region of the animal as seen on the frame captured by the tracking camera, θ is the rotation angle between the field of view of the tracking microscope and the sensor of the tracking camera, and r is the pixel size of the frames taken through the tracking camera. The velocity of the animal calculated by dividing the displacement vector of the animal between adjacent time points by the duration of the time interval.

Aligning calcium imaging data with behavioral data. As described in the Microscope Design and Assembly section, the trigger signal for the confocal laser was simultaneously sent to the computer controlling the tracking microscope. This computer thereby store two sets of time stamps, one for the laser illumination sequence and the other for the behavioral tracking video. Since the internal clock is the same, we can interpolate both the calcium activity data and the behavioral data onto the same time axis. Specifically, we interpolated both the calcium activity and behavior time series to obtain a common sampling frequency of 2 Hz.

Calcium signal extraction and pre-processing. The fluorescent signal from each neuron in a given frame was calculated as the median of the brightest 100 pixels within the ROI (or all pixels if the size of the ROI was smaller than 100 pixels) of that neuron. This was done for both the green and the red channels. The following pre-processing steps were then applied to the time-series signals from both channels: 1) To reduce spurious noise, a sliding median filter with a window size of 5 frames were applied to the time series (Figure S2D). 2) To correct for the decay in fluorescent signal due to photobleaching, an exponential function was first fit to the time series. Next, the estimated exponential was normalized by its initial value and divided away from the denoised time series (Figure S2E). 3) The denoised and bleach-corrected time series from the green channel was divided by that from the red channel. The resulting ratio-metric signal was normalized such that the 1st percentile of the signal takes a value of 0 while the 99th percentile maps to 1. This normalized ratio-metric signal was used for all subsequent data analyses.

Principal component analysis (PCA). An *N-by-M* data matrix was assembled with the rows representing neuron identity ($N = 10$) and the columns time points. For each wild type data set, the calcium activity data from each neurons was represented as row vectors and concatenated

along the neuron dimension. Data across different recording sessions were concatenated along the time dimension. PCA was performed by first subtracting the mean from each row and then applying singular value decomposition to the matrix.

Cross-correlation in neural activity. To estimate the time-lagged similarity between the activity of two neurons for a given genotype, the cross-correlation function (XCF) was first calculated individually for each data set of that genotype and then averaged. Bootstrapping was done to obtain confidence intervals on the mean. To examine the functional coupling between two neurons over time (Fig. 3D and G), average XCFs were calculated for data from a series of 60 second time windows spanning from 90 seconds before NSM activation to 90 seconds after. For each time window, the point with the largest absolute value along the average XCF was identified. The mean and 95% CI values of these extrema points were concatenated chronologically to generate Fig. 3D and G. This process is exemplified in Figure S7.

Convolutional neural network (CNN) classifier. The classifier was implemented using the Deep Learning Toolbox in MATLAB. The architecture of the network consists of a single convolutional layer with a single channel of two 9-by-3 convolutional kernels with no padding, followed by a Rectified Linear Unit (ReLu) layer, a fully connected layer with two neurons, a two-way softmax layer and a classification output layer. The last layer is specifically required for the Matlab implementation and computes the cross-entropy loss. Calcium activity from all neurons imaged, except for the 5-HT neuron NSM, were used for training, validation and testing. To specifically predict transition from roaming to dwelling, only data during roaming were used to predict the onset of NSM activity. For each wild type data set, calcium activity during each roaming state was first down-sampled by applying a 30 second average filter starting from right before the onset of a dwelling state and going back in time to the beginning of the roaming state.

Each time point in the down-sampled data was assigned a label of 1 or 0: 1 if it is immediately prior to an episode of NSM activation, and 0 otherwise. Positive and negative samples were balanced by weighting the prediction error of each sample by the number of samples in that class. The positive and negative sample groups were each partitioned at random into the training, validation, and test sets at an 8:1:1 relative ratio. This random partition was repeated 200 times. For each data partition, network training was performed 10 times with random initial conditions, using Stochastic Gradient Descent with Moment (SGDM) with the following hyper-parameters:

Hyper-parameter name	Value
Initial Learning Rate	0.09
L2 Regularization Rate	0.0001
Learning Rate Drop Factor	0.1
Learning Rate Drop Period	10
Momentum	0.9
Validation Frequency	30
Max number of epochs	150

To identify convolutional kernels that consistently contribute to classifier accuracy, convolutional kernels from networks that achieved greater than 50% test accuracy were recorded and k-means clustering was performed. Within each cluster, the distribution of weights at each kernel location was used to extract a confidence interval for the mean value of that kernel element. Elements of the kernel with mean values significantly different from 0 were taken to indicate important neural activity profiles for predicting NSM activation. Since each kernel element maps to the activity of a given neuron at a particular time window, the preferred sign of a kernel element would suggest whether a neuron is preferentially active (when the preferred sign is positive) or inactive (when the preferred sign is negative) at that time window.

Feature selection was performed to identify key neurons whose activity critically contribute to classification accuracy. To generate the results in Fig. 3C, data from a chosen

neuron was removed from the 9-neuron data set, and the resulting partial data set was used to train CNNs following procedure described above. To generate the results in Figure S6B, two types of partial data sets were used. In the first category, data from 6 out of 9 neurons were used for training. We tested all possible 9-choose-6 neuron combinations. In second category, we tested using data from only RIB, AIA, and AVA for network training.

Data Analysis for Behavioral Assays

Extraction of locomotory parameters. Animal trajectories were first extracted using custom software described previously(Rhoades et al., 2019). Speed and angular speed were calculated for all time points of each trajectory, and then averaged over 10 second intervals.

Identification of roaming and dwelling states. Roaming and dwelling states were identified as previously described(Flavell et al., 2013). Briefly, the speed and angular speed measured for each animal at each time point was assigned into one of two clusters. This allowed each animal trajectory to be converted into a binary sequence. A two-state HMM was fit to these binary sequences to estimate the transition and emission probabilities. This was done separately for each genotype under each experimental condition.

Calculation of chemotaxis bias. The instantaneous chemotaxis bias $c(t)$ was defined as:

$$c(t) = \frac{(\boldsymbol{v} \cdot \boldsymbol{g})}{(\|\boldsymbol{v}\| \times \|\boldsymbol{g}\|)}$$

Where $\boldsymbol{v}$ is the instantaneous velocity of the animal, and $\boldsymbol{g}$ is the unit vector that points from the animal's current location to the nearest point on the boundary between the sparse food patch and the dense food patch. Here, $\boldsymbol{g}$ is used as the proxy for the gradient of olfactory cues at the animal's current location. Equivalently, $c(t)$ is the cosine of the angle between the animal's

instantaneous direction of motion and the direction of the chemotactic gradient at its current location.

QUANTIFICATION AND STATISTICAL ANALYSES

Comparison of sample means. The Wilcoxon ranksum test was applied pair-wise to obtain the raw p-values. When multiple comparisons were done for the same type of experiment (e.g. comparing the fraction of animal roaming during the Patch Foraging Assay for different genotypes), the Benjamini-Hochberg correction was used to control the false discovery rate. A corrected p-value less than 0.05 was considered significant.

Bootstrap confidence intervals. Bootstrapping was performed by sampling with replacement *N* times from the original data distribution (*N* equals the size of the original distribution). This procedure was repeated 1000 times and the test statistic of interest (e.g. the sample mean) was calculated each time on the bootstrapped data. The 5th and 95th percentiles of the calculated values then constitute the lower and upper bounds of the 95% confidence interval.

Author Contributions

N.J. and S.W.F conceived of the study. N.J., G.K.M., and S.W.F. designed/performed experiments and performed data analysis. N.J., G.I.F., and A.D. designed and wrote software. C.M.B., and I.N. performed experiments and analyzed data.

Declaration of Interests

The authors declare no competing interests.

Acknowledgments

We thank Rachel Wilson, Andrew Gordus, Paul Greer, and members of the Flavell lab for helpful comments on the manuscript. We thank Andrew Leifer for helpful advice and sharing software related to the tracking microscope and Nate Cermak for help with hardware control on the tracking microscope. We thank the Bargmann lab and the *Caenorhabditis* Genetics Center (supported by P40 OD010440) for strains. N.J. acknowledges support from the Picower Fellows program and the Charles King Trust Postdoctoral Fellowship. S.W.F. acknowledges funding from the JPB Foundation, PIIF, PNDRF, the NARSAD Young Investigator Award Program, NIH (R01NS104892) and NSF (IOS 1845663 and DUE 1734870).

References

Acar, M., Mettetal, J.T., and van Oudenaarden, A. (2008). Stochastic switching as a survival strategy in fluctuating environments. Nat. Genet. *40*, 471–475.

Ache, J.M., Namiki, S., Lee, A., Branson, K., and Card, G.M. (2019). State-dependent decoupling of sensory and motor circuits underlies behavioral flexibility in Drosophila. Nat. Neurosci. *22*.

Andalman, A.S., Burns, V.M., Lovett-barron, M., Levoy, M., Rajan, K., Deisseroth, K., Andalman, A.S., Burns, V.M., Lovett-barron, M., Broxton, M., et al. (2019). Neuronal Dynamics Regulating Brain and Behavioral Neuronal Dynamics Regulating Brain and Behavioral State Transitions. Cell *177*, 1–16.

Anderson, D.J. (2016). Circuit modules linking internal states and social behaviour in flies and mice. Nat. Rev. Neurosci. *17*, 692–704.

Arous, J. Ben, Laffont, S., and Chatenay, D. (2009). Molecular and Sensory Basis of a Food Related Two-State Behavior in C. elegans. PLoS One *4*, 1–8.

Artiushin, G., and Sehgal, A. (2017). The Drosophila circuitry of sleep–wake regulation. Curr. Opin. Neurobiol. *44*, 243–250.

Bargmann, C.I. (2012). Beyond the connectome: how neuromodulators shape neural circuits. Bioessays *34*, 458–465.

Bartumeus, F., and Catalan, J. (2009). Optimal search behavior and classic foraging theory.

Beaumont, H., Gallie, J., Kost, C., Ferguson, G., and Rainey, P. (2009). Experimental evolution of bet hedging. Nature *462*, 90–93.

Brenner, S. (1974). The Genetics of Caenorhabditis elegans. Genetics *77*, 71–94.

Breton-Provencher, V., and Sur, M. (2019). Active control of arousal by a locus coeruleus GABAergic circuit. Nat. Neurosci. *22*, 218–228.

Brockmann, H.J. (1987). What is Bet-Hedging. In Oxford Surveys in Evolutionary Biology, Vol. 4, P.H. Harvey, and L. Partridge, eds. (Oxford University Press), pp. 182–211.

Chalasani, S.H., Chronis, N., Tsunozaki, M., Gray, J.M., Ramot, D., Goodman, M.B., and Bargmann, C.I. (2007). Dissecting a circuit for olfactory behaviour in Caenorhabditis elegans. Nature *450*, 63–70.

Chew, Y.L., Tanizawa, Y., Cho, Y., Zhao, B., Yu, A.J., Ardiel, E.L., Rabinowitch, I., Bai, J., Rankin, C.H., Lu, H., et al. (2018). An Afferent Neuropeptide System Transmits Mechanosensory Signals Triggering Sensitization and Arousal in C. elegans. Neuron *99*, 1233–1246.e6.

Choi, S., Chatzigeorgiou, M., Taylor, K.P., Schafer, W.R., and Kaplan, J.M. (2013). Analysis of NPR-1 Reveals a Circuit Mechanism for Behavioral Quiescence in C. elegans. Neuron *78*, 869–880.

Choi, S., Taylor, K.P., Chatzigeorgiou, M., Hu, Z., Schafer, W.R., and Kaplan, J.M. (2015). Sensory Neurons Arouse C. elegans Locomotion via Both Glutamate and Neuropeptide Release. PLoS Genet. *11*, 1–20.

Clowney, E.J., Iguchi, S., Bussell, J.J., Scheer, E., and Ruta, V. (2015). Multimodal Chemosensory Circuits Controlling Male Courtship in Drosophila. Neuron *87*, 1036–1049.

Cohen, J.D., McClure, S.M., and Yu, A.J. (2007). Should I stay or should I go? How the human brain manages the trade-off between exploitation and exploration. Philos. Trans. R. Soc. B Biol. Sci. *362*, 933–942.

Dobosiewicz, M., Liu, Q., and Bargmann, C.I. (2019). Reliability of an interneuron response depends on an integrated sensory state. Elife *8*.

Faumont, S., and Lockery, S.R. (2006). The awake behaving worm: Simultaneous imaging of neuronal activity and behavior in intact animals at millimeter scale. J. Neurophysiol.

Flavell, S.W., Pokala, N., Macosko, E.Z., Albrecht, D.R., Larsch, J., and Bargmann, C.I. (2013). Serotonin and the neuropeptide PDF initiate and extend opposing behavioral states in C. elegans. Cell *154*.

Fujiwara, M., Sengupta, P., and Mcintire, S.L. (2002). Regulation of Body Size and Behavioral State of C . elegans by Sensory Perception and the EGL-4 cGMP-Dependent Protein Kinase. *36*, 1091–1102.

Gallagher, T., Bjorness, T., Greene, R., You, Y., and Avery, L. (2013). The Geometry of Locomotive Behavioral States in C . elegans. *8*.

Goldman, M.S., Compte, A., and Wang, X. (2007). Theoretical and computational neuroscience: Neural integrators: recurrent mechanisms and models. Squire, L.; Albright, T.; Bloom. F.

Gutierrez, G.J., Leary, T.O., and Marder, E. (2013). Viewpoint Multiple Mechanisms Switch an

Electrically Coupled , Synaptically Inhibited Neuron between Competing Rhythmic Oscillators. Neuron *77*, 845–858.

Hoopfer, E.D., Jung, Y., Inagaki, H.K., Rubin, G.M., Anderson, D.J., and Hoopfer, Jung, Rubin, A. (2015). P1 interneurons promote a persistent internal state that enhances inter-male aggression in Drosophila. Elife *1*, 1689–1699.

Inagaki, H.K., Fontolan, L., Romani, S., and Svoboda, K. (2019). Discrete attractor dynamics underlies persistent activity in the frontal cortex. Nature *566*, 212–217.

Jovanic, T., Schneider-mizell, C.M., Shao, M., Truman, J.W., Cardona, A., Zlatic, M., Jovanic, T., Schneider-mizell, C.M., Shao, M., Masson, J., et al. (2016). Competitive Disinhibition Mediates Behavioral Choice and Sequences in Drosophila. Cell 1–13.

Kato, S., Kaplan, H.S., Schrödel, T., Skora, S., Lindsay, T.H., Yemini, E., Lockery, S., and Zimmer, M. (2015). Global Brain Dynamics Embed the Motor Command Sequence of Caenorhabditis elegans. Cell *163*, 656–669.

Kim, S.S., Hermundstad, A.M., Romani, S., Abbott, L.F., and Jayaraman, V. (2019). Generation of stable heading representations in diverse visual scenes. Nature *576*.

Komatsu, H., Mori, I., and Rhee, J. (1996). Mutations in a Cyclic Nucleotide-Gated Channel Lead to Abnormal Thermosensation and Chemosensation in C. elegans. Neuron *17*, 707–718.

Kussell, E., and Leibler, S. (2005). Phenotypic diversity, population growth, and information in fluctuating environments. Science *309*, 2075–2078.

Larsch, J., Flavell, S.W., Liu, Q., Gordus, A., Albrecht, D.R., and Bargmann, C.I. (2015). A Circuit for Gradient Climbing in C. elegans Chemotaxis. Cell Rep. *12*, 1748–1760.

Lee, S.H., and Dan, Y. (2012). Neuromodulation of Brain States. Neuron *76*, 109–222.

Li, N., Daie, K., Svoboda, K., and Druckmann, S. (2016). Robust neuronal dynamics in premotor cortex during motor planning.

Li, Z., Liu, J., Zheng, M., and Xu, X.Z.S. (2014). Encoding of Both Analog- and Digital-like Behavioral Outputs by One C. elegans Interneuron. Cell *159*, 751–765.

Machens, C.K., Romo, R., and D., B.C. (2005). Flexible Control of Mutual Inhibition: A Neural Model of Two-Interval Discrimination. Science (80-.). *34*, 1121–1124.

Maimon, G. (2011). Modulation of visual physiology by behavioral state in monkeys , mice , and flies. Curr. Opin. Neurobiol. *21*, 559–564.

Major, G., and Tank, D. (2004). Persistent neural activity: Prevalence and mechanisms. Curr. Opin. Neurobiol. *14*, 675–684.

Marder, E. (2012). Neuromodulation of Neuronal Circuits: Back to the Future. Neuron *76*, 1–11.

Nguyen, J.P., Shipley, F.B., Linder, A.N., Plummer, G.S., Liu, M., Setru, S.U., Shaevitz, J.W., and Leifer, A.M. (2016). Whole-brain calcium imaging with cellular resolution in freely behaving Caenorhabditis elegans. Proc. Natl. Acad. Sci. *113*, E1074–E1081.

Nichols, A.L.A., Eichler, T., Latham, R., and Zimmer, M. (2017). A global brain state underlies C. elegans sleep behavior. Science (80-.). *356*.

Rengarajan, S., Yankura, K.A., Guillermin, M.L., Fung, W., and Hallem, E.A. (2019). Feeding

state sculpts a circuit for sensory valence in Caenorhabditis elegans. Proc. Natl. Acad. Sci. *116*.

Rhoades, J.L., Nelson, J.C., Nwabudike, I., Yu, S.K., McLachlan, I.G., Madan, G.K., Abebe, E., Powers, J.R., Colón-Ramos, D.A., and Flavell, S.W. (2019). ASICs Mediate Food Responses in an Enteric Serotonergic Neuron that Controls Foraging Behaviors. Cell *176*, 85–97.e14.

Roberts, W.M., Augustine, S.B., Lawton, K.J., Lindsay, T.H., Thiele, T.R., Izquierdo, E.J., Faumont, S., Lindsay, R.A., Britton, M.C., Pokala, N., et al. (2016). A stochastic neuronal model predicts random search behaviors at multiple spatial scales in C . elegans. 1–41.

Romo, R., Machens, C.K., and Brody, C.D. (2005). Flexible Control of Mutual Inhibition: A Neural Model of Two-Interval Discrimination (Supporting Methods). Science (80-.). *34*, 1121–1125.

Sawin, E.R., Ranganathan, R., and Horvitz, H.R. (2000). C. elegans locomotory rate is modulated by the environment through a dopaminergic pathway and by experience through a serotonergic pathway. Neuron *26*.

Schwarz, L.A., and Luo, L. (2015). Organization of the locus coeruleus-norepinephrine system. Curr. Biol. *25*, R1051–R1056.

Seo, C., Guru, A., Jin, M., Ito, B., Sleezer, B.J., Ho, Y.Y., Wang, E., Boada, C., Krupa, N.A., Kullakanda, D.S., et al. (2019). Intense threat switches dorsal raphe serotonin neurons to a paradoxical operational mode. Science (80-.). *363*, 539–542.

Seung, H.S. (1996). How the brain keeps the eyes still. Proc. Natl. Acad. Sci. U. S. A. *93*, 13339–13344.

Shtonda, B.B., and Avery, L. (2006). Dietary choice behavior in Caenorhabditis elegans. J. Exp. Biol. *209*, 89–102.

Spencer, W.C., Mcwhirter, R., Miller, T., Strasbourger, P., Thompson, O., Hillier, L.W., Waterston, R.H., and Iii, D.M.M. (2014). Isolation of Specific Neurons from C. elegans Larvae for Gene Expression Profiling. PLoS One *9*, 1–11.

Sutton, R.S., and Barto, A.G. (2018). Reinforcement Learning (Bradford).

Suzuki, H., Thiele, T.R., Faumont, S., Ezcurra, M., Lockery, S.R., and Schafer, W.R. (2008). Functional asymmetry in Caenorhabditis elegans taste neurons and its computational role in chemotaxis. Nature *454*, 114–117.

Tan, R.Z., Ji, N., Mentink, R. a, Korswagen, H.C., and van Oudenaarden, A. (2013). Deconvolving the roles of Wnt ligands and receptors in sensing and amplification. Mol. Syst. Biol. *9*, 631.

Thiele, T.R., Bargmann, C.I., Lockery, S.R., Roberts, W.M., Pokala, N., Britton, M.C., Lindsay, T.H., Lawton, K.J., Lindsay, R.A., Izquierdo, E.J., et al. (2016). A stochastic neuronal model predicts random search behaviors at multiple spatial scales in C. elegans. Elife *5*, 1–41.

Tsalik, E.L., and Hobert, O. (2003). Functional mapping of neurons that control locomotory behavior in Caenorhabditis elegans. J. Neurobiol. *56*, 178–197.

Venkatachalam, V., Ji, N., Wang, X., Clark, C., Kameron, J., and Klein, M. (2015). Pan-neuronal imaging in roaming Caenorhabditis elegans. Proc. Natl. Acad. Sci. *113*.

Vergassola, M., Villermaux, E., and Shraiman, B.I. (2007). “Infotaxis” as a strategy for

searching without gradients. Nature *445*, 406–409.

Wang, X.-J. (2012). Neural dynamics and circuit mechanisms of decision-making. Curr. Opin. Neurobiol. *22*, 1039–1046.

Wang, X.J. (2001). Synaptic reverberation underlying mnemonic persistent activity. Trends Neurosci. *24*, 455–463.

Wang, X.J. (2002). Probabilistic decision making by slow reverberation in cortical circuits. Neuron *36*, 955–968.

Watanabe, K., Chiu, H., Pfeiffer, B.D., Wong, A.M., Hoopfer, E.D., Rubin, G.M., Anderson, D.J., Watanabe, K., Chiu, H., Pfeiffer, B.D., et al. (2017). A Circuit Node that Integrates Convergent Input from Neuromodulatory and Social Behavior-Promoting Neurons to Control Aggression in Drosophila. Neuron *95*, 1112–1128.e7.

Weissbourd, B., Ren, J., DeLoach, K.E., Guenthner, C.J., Miyamichi, K., and Luo, L. (2014). Presynaptic Partners of Dorsal Raphe Serotonergic and GABAergic Neurons. Neuron *83*, 645–662.

White, J.G., Southgate, E., Thomson, J.N., and Brenner, S. (1986). The structure of the nervous system of the namtode Caenorhabditis elegans. Philos. Trans. R. Soc. London B *314*.

Xiong, W., and Ferrell Jr, J.E. (2003). A positive-feedback-based bistable " memory module " that governs a cell fate decision. Nature *426*, 460–465.

Figure Legends

Figure 1. Circuit-wide calcium imaging reveals stable, low-dimensional neural representation of foraging states. (A) Example of worm behavior during calcium imaging, shown as movement path (top) and speed trace (bottom). Red and black dots mark beginning and end of path, respectively. (B) Neural circuit that is proposed to control roaming and dwelling states. Each *C. elegans* neuron has a three-letter name; gray arrows indicate connections from wiring diagram; blue and orange arrows indicate neuromodulatory connections from Flavell et al., 2013. (C) Example wild-type dataset from multi-neuron calcium imaging. Each neuron's calcium trace is in black. Background colors indicate axial velocity of the animal, and the behavioral state of the animal is indicated at top. GCaMP6m data were divided by co-expressed mScarlett fluorescence levels and normalized to the fifth percentile of the activity for each

neuron (R_0). (D) Average activity of each neuron during forward vs. reverse movement, and dwelling vs. roaming. Data are from 17 animals and are shown as means and their 95% confidence interval (95% CI). **p<0.01; ****p<0.001, Wilcoxon ranksum test. (E) Scatterplots projecting neural activity data into principal component space. Data are from 17 animals and are colored according to the ongoing axial velocity (left) or foraging state (right). (F) Scatterplots projecting neural activity into PC space. Data are from 17 animals and colored by ongoing NSM activity. Here, NSM activity was normalized to a 0-1 scale for each animal. (G) Scatterplot depicting relationship of NSM activity and animal speed. Individual data points are from 17 animals and are colored according to the behavioral state of the animal. (H) Event-triggered averages centered on NSM activation (left) and termination (right) events. Data are from 17 animals and are shown as mean and 95% CI. PC4 is shown alongside PC1 and PC2 to indicate that neural dynamics beyond the first two principal components also change coincident to NSM activation. (I) Average trajectory in principal component space during moments of NSM activation, i.e. during roaming-to-dwelling transitions. Arrows represent average activity dynamics over 15 second intervals. Color indicates ongoing NSM activity. Faint lines show bootstrap samples to estimate variability.

Figure 2. Serotonin signaling promotes persistent activation of serotonergic NSM neurons via a mutual inhibitory circuit. (A-B) Example circuit-wide calcium imaging datasets from *tph-1* (A) and *mod-1* (B) mutant animals, shown as in Fig. 1C. (C-D) Scatterplots of NSM and AVB activity in WT (C) and 5-HT pathways mutants, *tph-1* and *mod-1* (D). Each data point is colored by the ongoing foraging state of animal (roaming: orange, dwelling: blue). Insets show the relative density of data points in the four quadrants of the graph (see scale bar to the far

right). (E) Fraction of time roaming versus dwelling for the indicated genotypes. Error bars depict 95% CI. (F) Duration of NSM activation events in the indicated genotypes, shown as means and 95% CI. ****p<0.0001, Wilcoxon ranksum test. For (C-F), N = 17, 10, and 8 animals for WT, *tph-1*, and *mod-1*, respectively. (G) Circuit schematic based on results from the *tph-1* and *mod-1* mutants, showing cross inhibition between the 5-HT neuron NSM and the MOD-1 expressing neurons.

Figure 3. PDF signaling is required for mutual exclusivity between circuit states and acts downstream of the 5-HT target neurons in the mutual inhibitory circuit. (A) Example circuit-wide calcium imaging dataset from *pdfr-1* mutants lacking PDF neuropeptide signaling, shown as in Fig. 1C. No roaming/dwelling ethogram is shown because the overall speed distribution was strongly altered in this mutant (see Fig. 2J). (B) Example circuit-wide calcium imaging dataset from transgenic animals expressing the hyperactive PDFR-1 effector ACY-1(P260S) specifically in PDFR-1 expressing neurons. (C) Scatterplots of NSM and AVB activity in *pdfr-1* mutants, transgenic *pdfr-1::acy-1(P260S)gf* animals, and *tph-1; pdfr-1* double mutants. Data points are colored by the ongoing foraging state (roaming: orange, dwelling: blue). Insets show the relative density of data points in the four quadrants of the graph. (D) Histograms depicting animal speed distributions for the indicated genotypes. Solid vertical lines depict the means; dashed lines in lower panels are WT means. (E) Duration of NSM activation events in the indicated genotypes shown as mean and 95% CI. *p<0.05, Wilcoxon ranksum test. For (C-E), N = 11, 9 and 8 animals for *pdfr-1*, *pdfr-1::acy-1gf*, and *tph-1;pdfr-1* animals.(F) Speed of wild type and *pdfr-1* mutant animals in response to optogenetic activation of the MOD-1 expressing neurons (red shading). (G) Circuit schematic summarizing results shown in (C-F).

The PDFR-1 expressing neurons act downstream of the MOD-1 expressing neurons to inhibit the 5-HT neuron NSM. Dotted box indicates the canonical sensorimotor pathway.

Figure 4. Training a CNN classifier identifies circuit activity patterns predictive of roaming-to-dwelling state transitions. (A) Examples (left and center) and event-triggered averages (right) showing each neuron's activity during moments of NSM activation. Data in event-triggered averages are means and 95% CI. Red arrowheads indicate significant change in activity between 90-80 seconds versus 10-0 seconds prior to NSM activation. (B) Schematic illustrating the architecture of the Convolutional Neural Network (CNN) trained to predict NSM activation events. (C) Left: a common convolutional kernel found across successfully trained CNNs. Only weights that are significantly different from zero are colored. Right: Average area under the curve for the Receiver Operating Characteristic curve (AUC-ROC) from networks trained using data from 8-out-of-9 neurons at a time. Error bars are 95% CI of the mean. Vertical gray stripe denotes the 95% CI of the AUC-ROC from networks trained using data from all 9 neurons. **$p<0.01$, Wilcoxon ranksum test.

Figure 5. The AIA sensory processing neuron can couple to both the roaming and dwelling networks and controls state switching. (A) Maximal cross-correlation coefficients between AIA and the indicated neurons around the time of NSM activation. See Figure S5 for example cross-correlation functions whose maxima were used to construct the curves in the current plot. (B) Scatterplots showing activities of AIA and RIB during periods of NSM inactivity (gray dots) and within 30-0 seconds prior to NSM activation (orange dots). Each data point represents the average activity of the indicated neurons in a 5 second interval. Marginal distribution of each

neuron is depicted along the x- or the y-axes. ***p<0.001, Wilcoxon ranksum test. (C) Ratio between the activities of AIA and RIB (i.e. the y/x values for the data points shown in (B)) during periods of NSM inactivity (gray) and within 30-0 seconds prior to NSM activation (orange). Data are shown as means and 95% CI. ****p<0.0001, Wilcoxon ranksum test. (D-F) Relationships between the activities of AIA and NSM, depicted as in (A-C) except for blue data points in (E) and blue bar in (F) correspond to data from 0-30 seconds after NSM activation. For (A-F), n= 17 WT animals. (G) Average animal speed before, during, and after AIA::Chrimson activation. Animals were separately analyzed based on whether they were roaming (orange) or dwelling (blue) prior to AIA stimulation. N=1032 wild type animals. Gray lines indicate no-all-trans-retinal controls. N=370 no-ATR control animals. (H) Effects of AIA stimulation in *tph-1* mutant animals, depicted as in (G). N= 927 *tph-1* mutant animals and N = 284 no-ATR control animals. (I) Effects of AIA stimulation in *pdfr-1* mutant animals, depicted as in (G). Note that *pdfr-1* animals do not roam enough to examine AIA-induced slowing. N= 383 *pdfr-1* mutant animals and N = 237 no-ATR control animals. (J) Functional architecture of the circuit controlling the roaming and dwelling states, based on results from Figures 2-5.

Figure 6. The AIA sensory processing neuron couples dynamic olfactory cues to behavioral states. (A) Top: cartoon depicting patch foraging behavioral assay. Bottom: example of two *C. elegans* movement paths from a patch foraging assay, where paths are colored by speed. Red dots indicate beginnings of movement paths. (B) Fraction of animals roaming on sparse side of patch assay plates versus control sparse food plates that lack a nearby dense food patch. Error bars denote 95% CI. (C) Cartoon depicting how “chemotaxis bias” (i.e. the extent to which the animal’s locomotion was directed up the food odor gradient) is calculated. Inset compass shows

chemotaxis bias values for four orthogonal directions relative to dense food patch. (D) Average chemotaxis bias during roaming versus dwelling while animals navigate on patch assay plates (dark gray) or on control sparse food plates that lack a nearby dense food patch (light gray). Data are shown as mean and 95% CI. (E) Average chemotaxis bias surrounding transitions from roaming into dwelling states. Dark gray indicates wild type animals on patch assay plates, while light gray is control plates with uniform sparse food. Data are shown as mean and 95% CI. (F) Cross-correlation between animal speed and chemotaxis bias. The lagged correlation indicates that chemotaxis bias changes before speed. Data are shown as means ± SEM. For (B-F), n = 288 animals on patch assay plates and 194 animals on control sparse food plates. (G-H) Fraction of animals roaming and chemotaxis bias during roaming, shown for the indicated genotypes. (I) Average chemotaxis bias surrounding dwelling state onset in wild type (black) versus *tax-4* (red), *AIA::unc-103gf* (green), *pdfr-1* (blue), and *tph-1* (yellow) animals on patch assay plates, shown as in (E). n = 81, 197, 99, and 212 animals for *tax-4*, *AIA::unc-103gf*, *pdfr-1*, and *tph-1*, respectively. (J) Cartoon depicting food exposure behavioral assay. (K) Fraction of time roaming versus dwelling and dwelling state durations for wild type and AIA-silenced animals exposed to uniformly-distributed bacterial lawns of sparse food (SF) or dense food (DF). Data are shown as mean and 95% CI. ****$p<0.0001$, Wilcoxon ranksum test. (L) Schematic of the functional circuit controlling roaming and dwelling during foraging.

Supplemental Figure Legends

Figure S1. Design and calibration of the spinning-disk confocal tracking scope. (A) Design of the microscope. Orange and green shaded boxes indicate the confocal and behavioral tracking parts of the microscope, respectively. An example image from the behavior tracking camera is

shown, with the worm outlined in white. mScarlett-expressing neurons can be robustly detected in the animal's head. (B) To minimize photo-bleaching, movement artifacts, and animal disturbance, the laser illumination of animals was timed to camera exposure and objective piezo movement during volume acquisition, as is illustrated. The tracking LED was also only illuminated in between GCaMP/mScarlett volume acquisitions, so as to prevent cross-talk between the upper and lower microscope paths. Laser illumination permitted animal tracking during volume acquisition. (C) A sample volume captured by the confocal microscope. Neurons expressing the GCaMP6m and the mScarlett fluorescent proteins are annotated. For AIY, the neurite is labeled. (D) Semi-automated segmentation of neuron boundaries using the SURF algorithm. For a subset of frames in a video, the neuron boundaries are manually outlined. Then, the boundaries are propagated from one frame to others, based on image transformations that are defined by matching SURF features across frames.

Figure S2. Calibration of behavioral tracking accuracy and the effect of motion on calcium imaging data. (A) Example trajectory of an animal recorded under the tracking confocal microscope. (B) An image of this animal's head region captured through the behavior tracking camera. Bright pixels correspond to neurons expressing the mScarlett transgene. (C) Probability distribution of the location of the head region as seen through the behavior tracking camera across all of the frames of the recording shown in (A). All scale bars in (A-C) represent 0.1 mm. (D-F) Extraction of calcium activity from dual-channel fluorescent intensities from a representative neuron. (D) Time series of red (emission wavelength 603-678nm) and green (emission wavelength 502-538nm) fluorescent intensities were first denoised by median filtering. (E) Next, photobleaching over time was corrected by fitting and then normalizing away an

exponential decay function. (F) Finally, the time series data from the green channels was divided by that from the red channel. The resulting time series was normalized to a relative scale of 0 to 1, with 0 corresponding to the 1st percentile and 1 to the 99th percentile of ratiometric values. (G) Range of variation normalized by mean calculated for the bleach-corrected red and green fluorescent intensities. Histograms were computed for aggregate data from all videos used in this study. Curved lines overlaying the red and green histograms (color matched) are mixture of Gaussian models fit to the corresponding histogram.

Figure S3. 5-HT and PDF signaling control circuit-wide dynamics. (A) Average trajectory in principal component space in response to optogenetic activation of NSM. Arrows represent average activity dynamics over 15 second intervals. Color indicates ongoing NSM activity. Faint lines show bootstrap samples to estimate variability. Black arrowheads indicate beginning and end of NSM::Chrimson activation. (B) Co-occurrence index for NSM and AVB activity in wild type and mutant animals during roaming and dwelling. Gray band indicates 95% CI of the index calculated for two i.i.d. Gaussian variables.

Figure S4. Evaluation of CNN classifiers trained on full or partial data, and connectivity of the AIA neuron that predicts NSM activation events. (A) AUC-ROC of the CNN classifiers trained on authentic data compared to those trained on scrambled data and to the performance of two other common types of classifiers. Data are shown as mean and 95% CI from 200 training sessions. (B) AUC-ROC of CNN classifiers trained on data withholding different neuron triplets from the full data set, or with data from only the RIB, AIA, and AVA neurons. Gray band indicate the 95% CI of the accuracy of CNN classifiers trained on the full data set, as shown in

A. (C) Synaptic inputs and outputs of the AIA neuron. Data are from the *C. elegans* connectome. Bilaterally symmetric pairs of neurons (e.g. AIAL and AIAR) were merged here for display purposes. Connections supported by only one single synapse were not included. Note the dense synaptic inputs onto AIA from chemosensory neurons.

Figure S5. AIA can functionally couple to either the roaming-active or the dwelling-active neurons and drive circuit state transition. (A) Average cross-correlation function between AIY and AIA activity at three time windows relative to NSM activation (from left to right): 1) 100 to 40.5 seconds prior, 2) 60 to 0.5 second prior, 3) 30 seconds prior to 30 seconds after (i.e. during NSM activity onset). (B) Average cross-correlation function between RIB and AIA activity during the same time windows as in (A). (C) Cross-correlation function between NSM and AIA activity during the same time windows as in (A). Red arrowheads denote the location of maximum absolute value of the average cross-correlation function. These values were used to generate the panels in Fig. 5A and Fig. 5D. Shaded regions denote 95% CI. (D) Top: Fraction of roaming animals exhibiting a drop in speed over during the first 10 seconds of optogenetic stimulation in wild type and mutant animals. Bottom: Fraction of dwelling animals exhibiting an increase in speed during the last 10 seconds of stimulation compared to pre-stimulation speeds. The no ATR results (dark gray) are shown to demonstrate the baseline state transitions that can occur during red light illumination. Note that *pdfr-1* animals do not roam enough to examine AIA-induced slowing. (E) NSM calcium signals and animal speed at moments of optogenetic AIA activation (red). For all panels, **$p<0.01$, ***$p<0.001$, ****$p<0.0001$, Wilcoxon ranksum test.

Figure S6. Chemotaxis performance in patch foraging assays. (A) Cross-correlation functions between instantaneous animal speed and chemotactic bias during the patch foraging assay for multiple mutant genotypes. Data are shown as means and 95% CI. (B) Trajectory of *tph-1* mutant animal in the patch foraging assay. Red dot indicates starting position. (C) AWA olfactory neurons elicit high-speed locomotion in an AIA-dependent manner. Average animal speed before, during (red shading), and after optogenetic AWA stimulation. Data for the indicated experimental groups are shown as means and 95% CI. (D) Average roaming state durations in wild type and AIA silenced animals exposed to uniformly distributed sparse food (SF) or dense food (DF). Data are shown as mean and 95% CI. **$p<0.01$, ***$p<0.001$, ****$p<0.0001$, Wilcoxon ranksum test.

Figure S7. Schematics depicting putative circuit activity states under different sensory contexts. (A) When the animal moves up a gradient of attractive cues, AIA receives strong input from its upstream sensory neurons. The outputs of AIA excite both the 5-HT neuron NSM and multiple MOD-1 and PDFR-1 expressing neurons in the sensorimotor pathway. Under this condition, the activity of the MOD-1 and PDFR-1 neurons may be high enough to dominate the mutual inhibitory circuit, leading to sustained inhibition of NSM and extended roaming states. (B) When the animal moves orthogonal to a gradient of attractive cues, excitatory input to AIA from its upstream sensory neurons may be weaker compared to the condition in (A). Both outputs of AIA may be reduced. The excitatory drive to NSM from food ingestion, however, remains unchanged. Under this condition, the activity of NSM may dominate the mutual inhibitory circuit, leading to an increase in time spent dwelling. (C) When the animal is exposed to uniformly-distributed sparse food, sensory neurons upstream of AIA are weakly activated due

to the lack of spatial and/or temporal concentration gradients. In contrast, NSM receives excitatory drive from ongoing food ingestion and biases the mutual inhibitory circuit towards the dwelling state. (D) When the animal is exposed to uniformly-distributed dense food, NSM may receive higher excitatory drive from increased rate of food ingestion, which further biases the mutual inhibitory circuit towards the dwelling state.

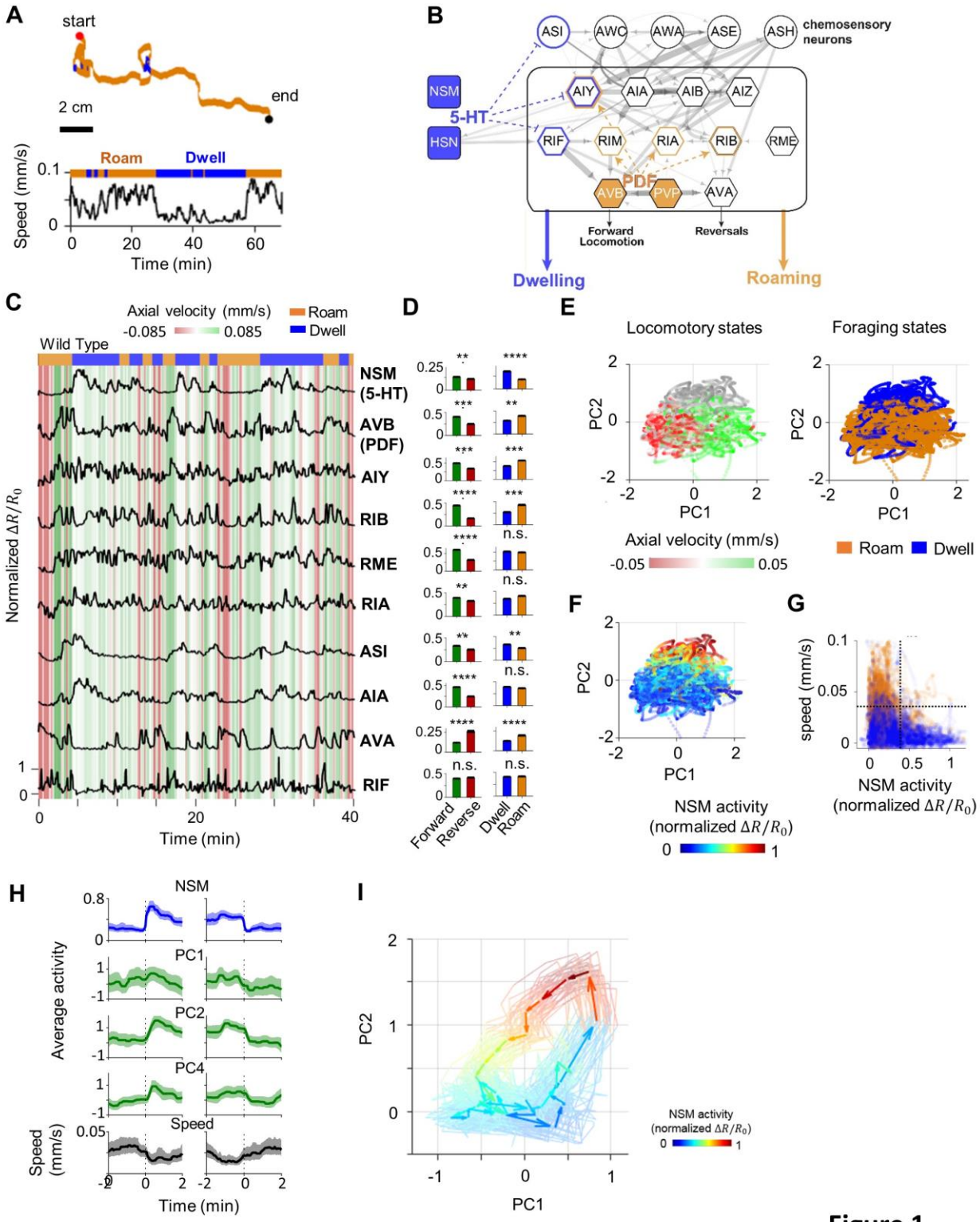
A
start
end
2 cm
Roam
Dwell
Speed (mm/s)
Time (min)
B
ASI
AWC
AWA
ASE
ASH
chemosensory neurons
NSM
5-HT
HSN
AIY
AIA
AIB
AIZ
RIF
RIM
RIA
RIB
RME
PDF
AVB
PVP
AVA
Forward Locomotion
Reversals
Dwelling
Roaming
C
Axial velocity (mm/s)
-0.085
0.085
Roam
Dwell
Wild Type
NSM (5-HT)
AVB (PDF)
AIY
RIB
RME
RIA
ASI
AIA
AVA
RIF
Normalized $\Delta R/R_0$
Time (min)
D
Forward
Reverse
Dwell
Roam
n.s.
E
Locomotory states
Foraging states
PC1
PC2
Axial velocity (mm/s)
-0.05
0.05
Roam
Dwell
F
NSM activity (normalized $\Delta R/R_0$)
G
speed (mm/s)
NSM activity (normalized $\Delta R/R_0$)
H
NSM
PC1
PC2
PC4
Speed
Average activity
Speed (mm/s)
Time (min)
I
PC1
PC2
NSM activity (normalized $\Delta R/R_0$)

Figure 1

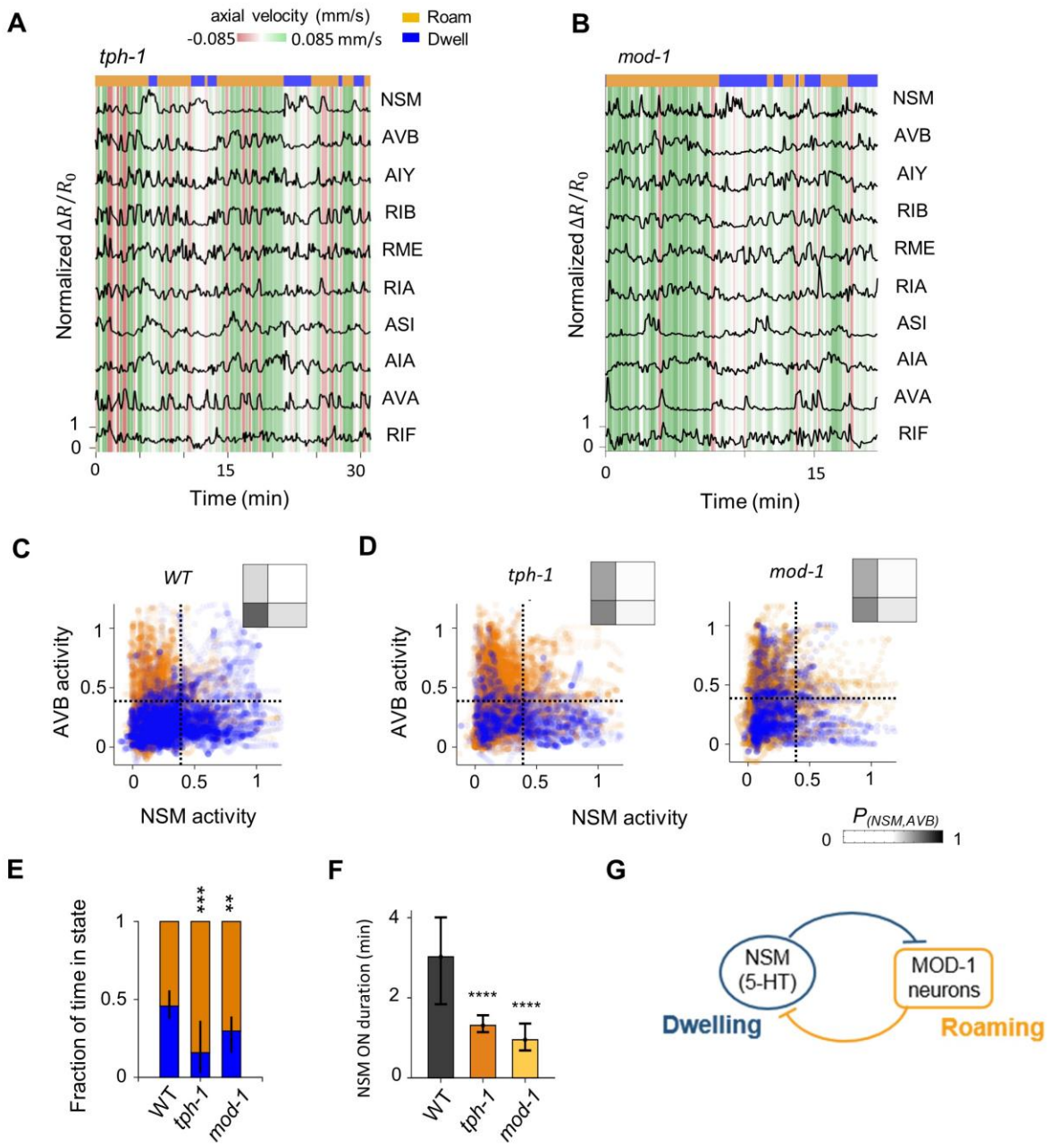
A
axial velocity (mm/s)
-0.085
0.085 mm/s
Roam
Dwell
tph-1
NSM
AVB
AIY
RIB
RME
RIA
ASI
AIA
AVA
RIF
Normalized ΔR / R0
Time (min)
B
mod-1
C
WT
AVB activity
NSM activity
D
tph-1
mod-1
P(NSM,AVB)
E
Fraction of time in state
WT
tph-1
mod-1
F
NSM ON duration (min)
G
NSM
(5-HT)
MOD-1
neurons
Dwelling
Roaming

Figure 2

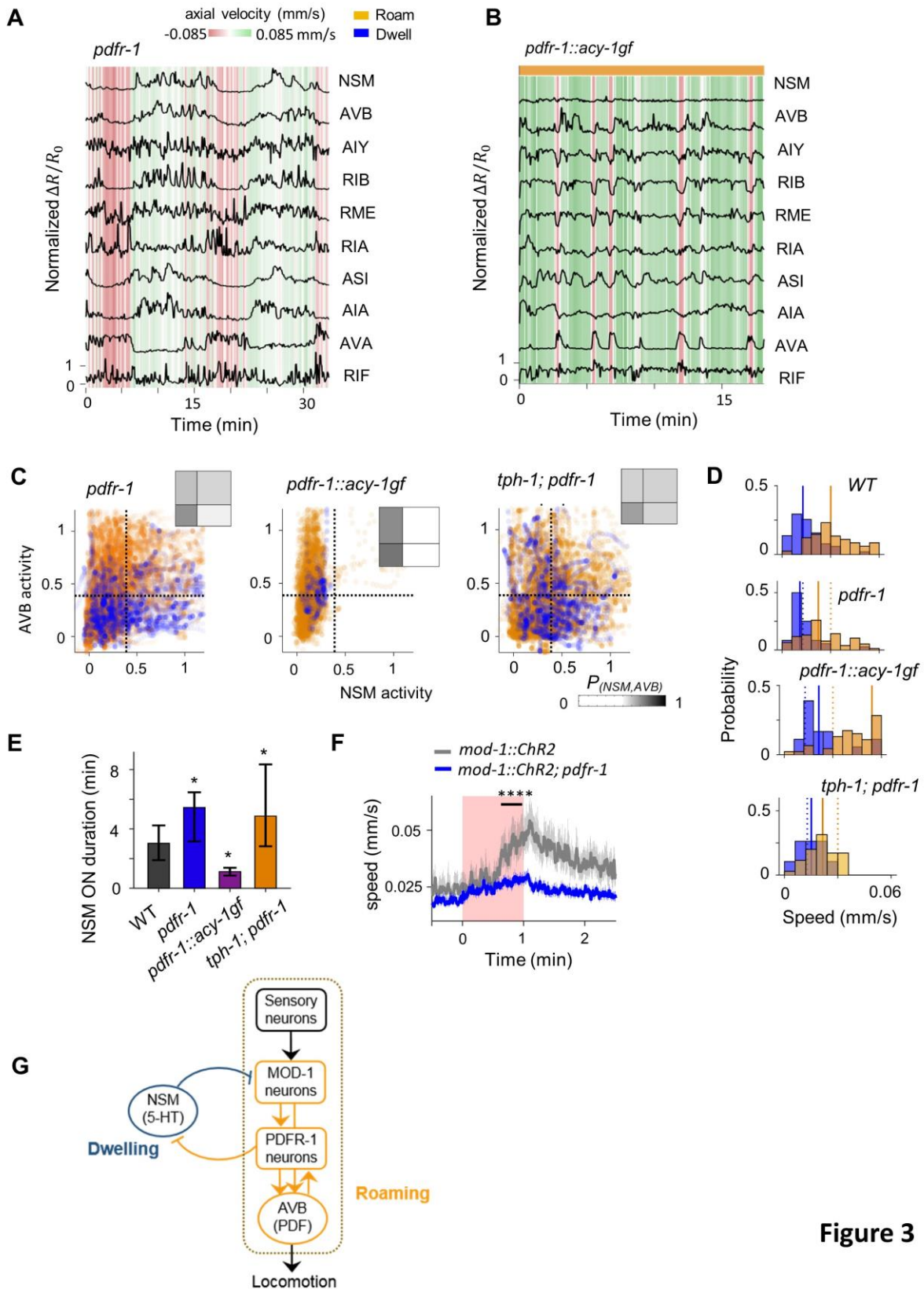
A
axial velocity (mm/s)
-0.085
0.085 mm/s
Roam
Dwell
pdfr-1
NSM
AVB
AIY
RIB
RME
RIA
ASI
AIA
AVA
RIF
Normalized $\Delta R/R_0$
Time (min)
B
pdfr-1::acy-1gf
C
pdfr-1
pdfr-1::acy-1gf
tph-1; pdfr-1
AVB activity
NSM activity
$P_{(NSM,AVB)}$
D
WT
pdfr-1
pdfr-1::acy-1gf
tph-1; pdfr-1
Probability
Speed (mm/s)
E
NSM ON duration (min)
WT
pdfr-1
pdfr-1::acy-1gf
tph-1; pdfr-1
F
mod-1::ChR2
mod-1::ChR2; pdfr-1
speed (mm/s)
Time (min)
G
Sensory neurons
MOD-1 neurons
NSM (5-HT)
Dwelling
PDFR-1 neurons
AVB (PDF)
Roaming
Locomotion

Figure 3

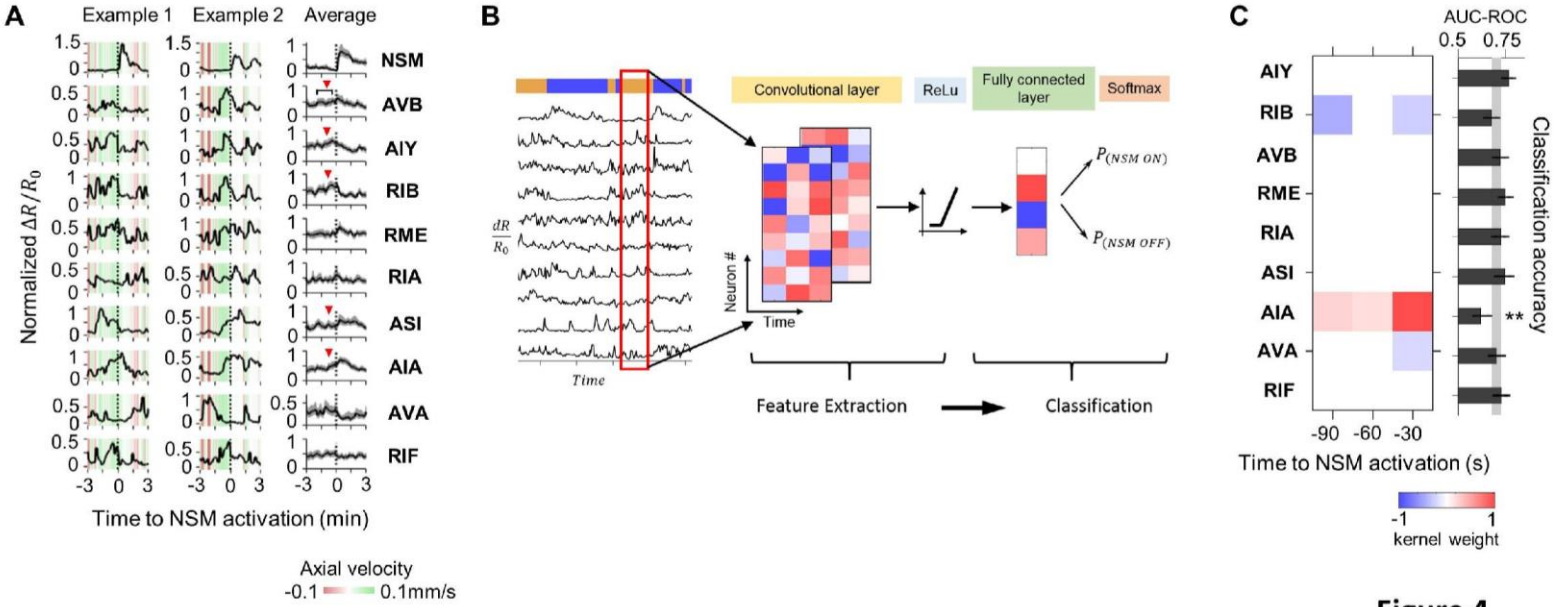
A
Example 1
Example 2
Average
NSM
AVB
AIY
RIB
RME
RIA
ASI
AIA
AVA
RIF
Normalized $\Delta R/R_0$
Time to NSM activation (min)
Axial velocity
-0.1
0.1mm/s
B
Convolutional layer
ReLu
Fully connected layer
Softmax
$\frac{dR}{R_0}$
Time
Neuron #
$P_{(NSM\ ON)}$
$P_{(NSM\ OFF)}$
Feature Extraction
Classification
C
AUC-ROC
0.5
0.75
Classification accuracy
**
Time to NSM activation (s)
-90
-60
-30
-1
1
kernel weight

Figure 4

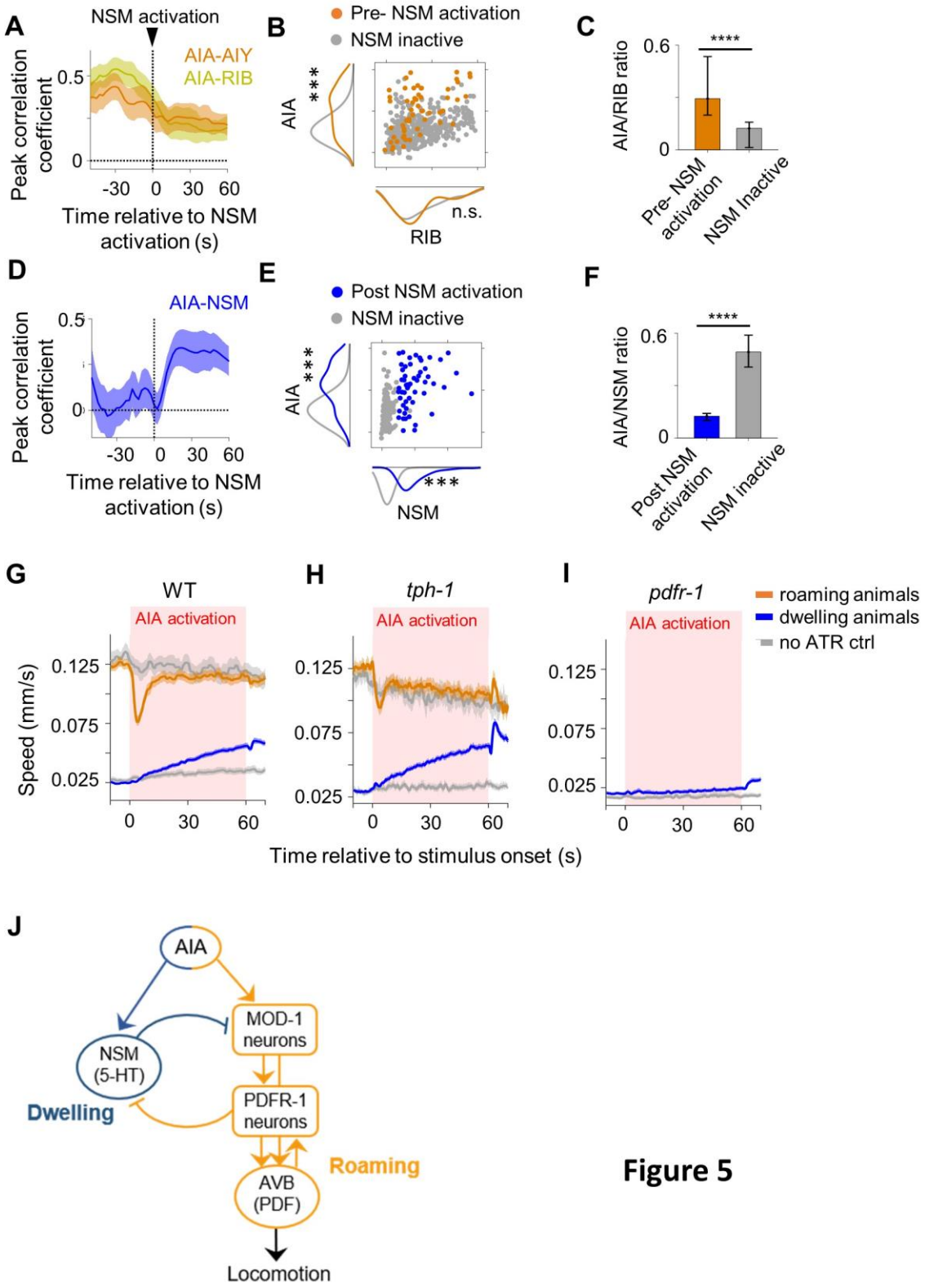
A
NSM activation
AIA-AIY
AIA-RIB
Peak correlation coefficient
0.5
0
-30 0 30 60
Time relative to NSM activation (s)
B
Pre- NSM activation
NSM inactive
AIA
***
n.s.
RIB
C
AIA/RIB ratio
0.6
0
****
Pre- NSM activation
NSM Inactive
D
AIA-NSM
Peak correlation coefficient
0.5
0
-30 0 30 60
Time relative to NSM activation (s)
E
Post NSM activation
NSM inactive
AIA
***
***
NSM
F
AIA/NSM ratio
0.6
0
****
Post NSM activation
NSM inactive
G
WT
AIA activation
Speed (mm/s)
0.125
0.075
0.025
0 30 60
H
tph-1
AIA activation
0.125
0.075
0.025
0 30 60
I
pdfr-1
AIA activation
roaming animals
dwelling animals
no ATR ctrl
0.125
0.075
0.025
0 30 60
Time relative to stimulus onset (s)
J
AIA
MOD-1 neurons
NSM (5-HT)
Dwelling
PDFR-1 neurons
Roaming
AVB (PDF)
Locomotion

Figure 5

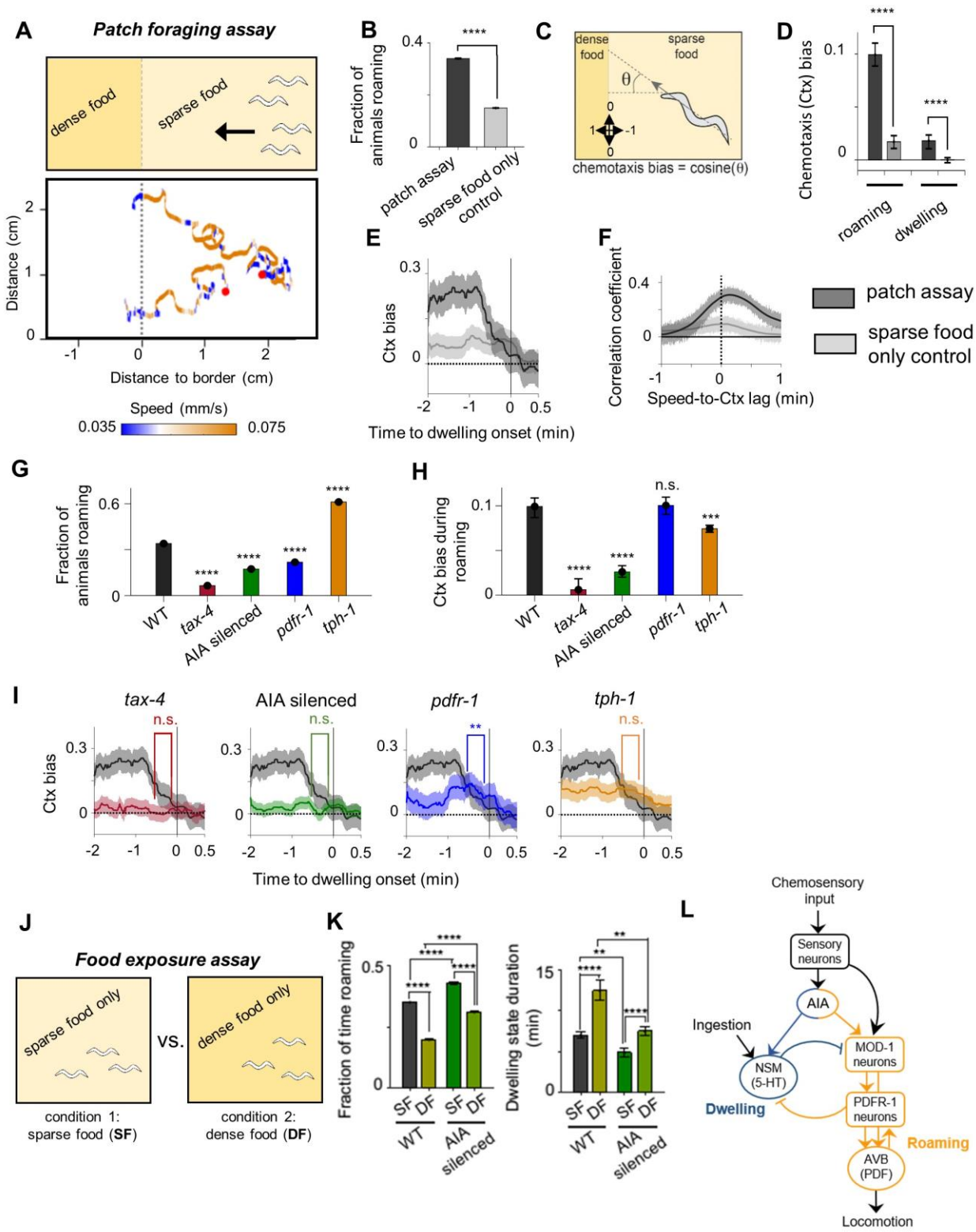
A
Patch foraging assay
dense food
sparse food
Distance (cm)
Distance to border (cm)
Speed (mm/s)
0.035
0.075
B
Fraction of animals roaming
patch assay
sparse food only control
C
dense food
sparse food
chemotaxis bias = cosine(θ)
D
Chemotaxis (Ctx) bias
roaming
dwelling
E
Ctx bias
Time to dwelling onset (min)
F
Correlation coefficient
Speed-to-Ctx lag (min)
patch assay
sparse food only control
G
Fraction of animals roaming
WT
tax-4
AIA silenced
pdfr-1
tph-1
H
Ctx bias during roaming
n.s.
I
tax-4
AIA silenced
pdfr-1
tph-1
Ctx bias
Time to dwelling onset (min)
J
Food exposure assay
sparse food only
vs.
dense food only
condition 1: sparse food (SF)
condition 2: dense food (DF)
K
Fraction of time roaming
Dwelling state duration (min)
SF
DF
WT
AIA silenced
L
Chemosensory input
Sensory neurons
AIA
Ingestion
NSM (5-HT)
MOD-1 neurons
Dwelling
PDFR-1 neurons
Roaming
AVB (PDF)
Locomotion

Figure 6

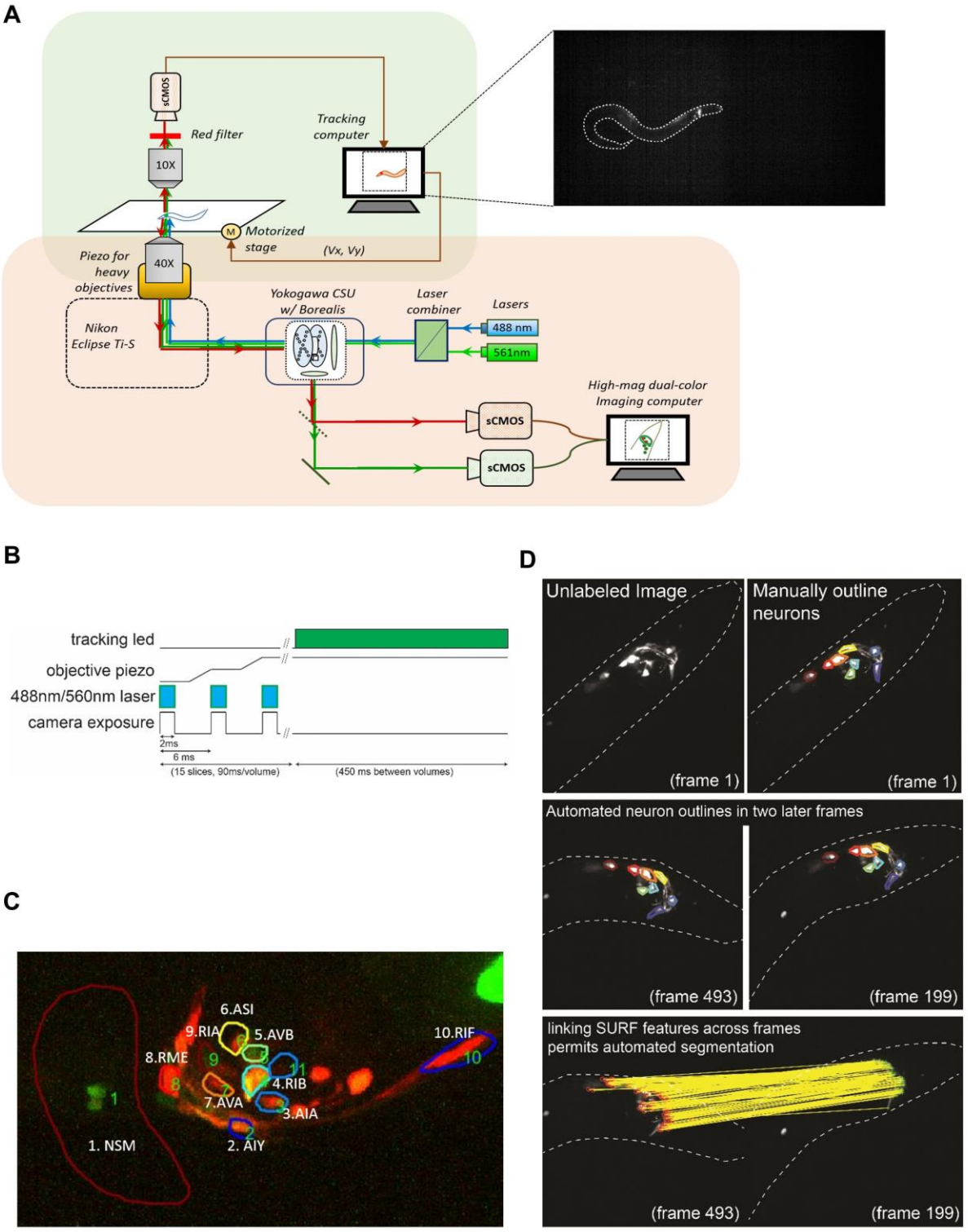
A
sCMOS
Red filter
10X
Tracking computer
Motorized stage
(Vx, Vy)
Piezo for heavy objectives
40X
Nikon Eclipse Ti-S
Yokogawa CSU w/ Borealis
Laser combiner
Lasers
488 nm
561nm
High-mag dual-color Imaging computer
sCMOS
sCMOS
B
tracking led
objective piezo
488nm/560nm laser
camera exposure
2ms
6 ms
(15 slices, 90ms/volume)
(450 ms between volumes)
C
6.ASI
9.RIA
5.AVB
10.RIF
8.RME
4.RIB
7.AVA
3.AIA
1. NSM
2. AIY
D
Unlabeled Image
Manually outline neurons
(frame 1)
(frame 1)
Automated neuron outlines in two later frames
(frame 493)
(frame 199)
linking SURF features across frames permits automated segmentation
(frame 493)
(frame 199)

Fig. S1

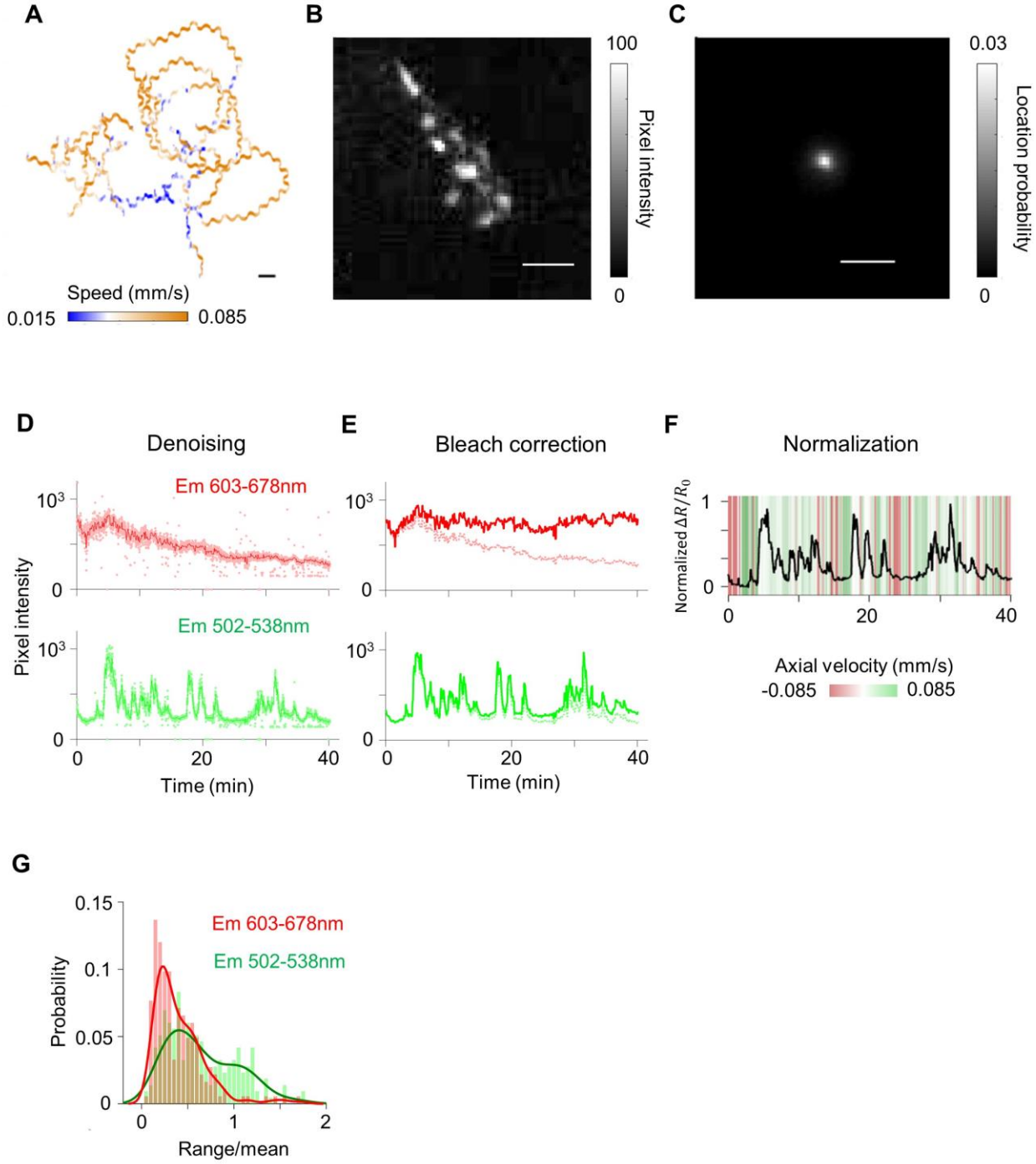
A
Speed (mm/s)
0.015
0.085
B
100
Pixel intensity
0
C
0.03
Location probability
0
D
Denoising
Em 603-678nm
Em 502-538nm
Pixel intensity
Time (min)
E
Bleach correction
Time (min)
F
Normalization
Normalized $\Delta R/R_0$
Axial velocity (mm/s)
-0.085
0.085
G
Em 603-678nm
Em 502-538nm
Probability
Range/mean

Fig. S2

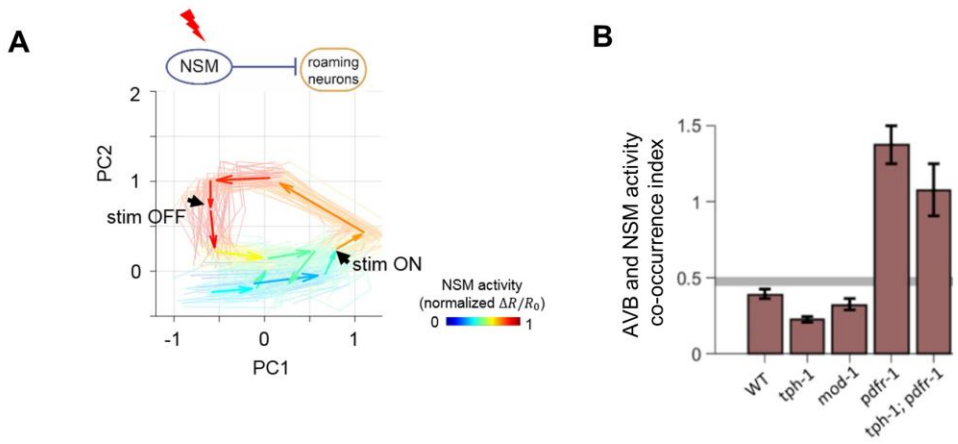
A
NSM
roaming neurons
PC2
PC1
stim OFF
stim ON
NSM activity
(normalized $\Delta R/R_0$)
0
1
B
AVB and NSM activity co-occurrence index
WT
tph-1
mod-1
pdfr-1
tph-1; pdfr-1

Fig. S3

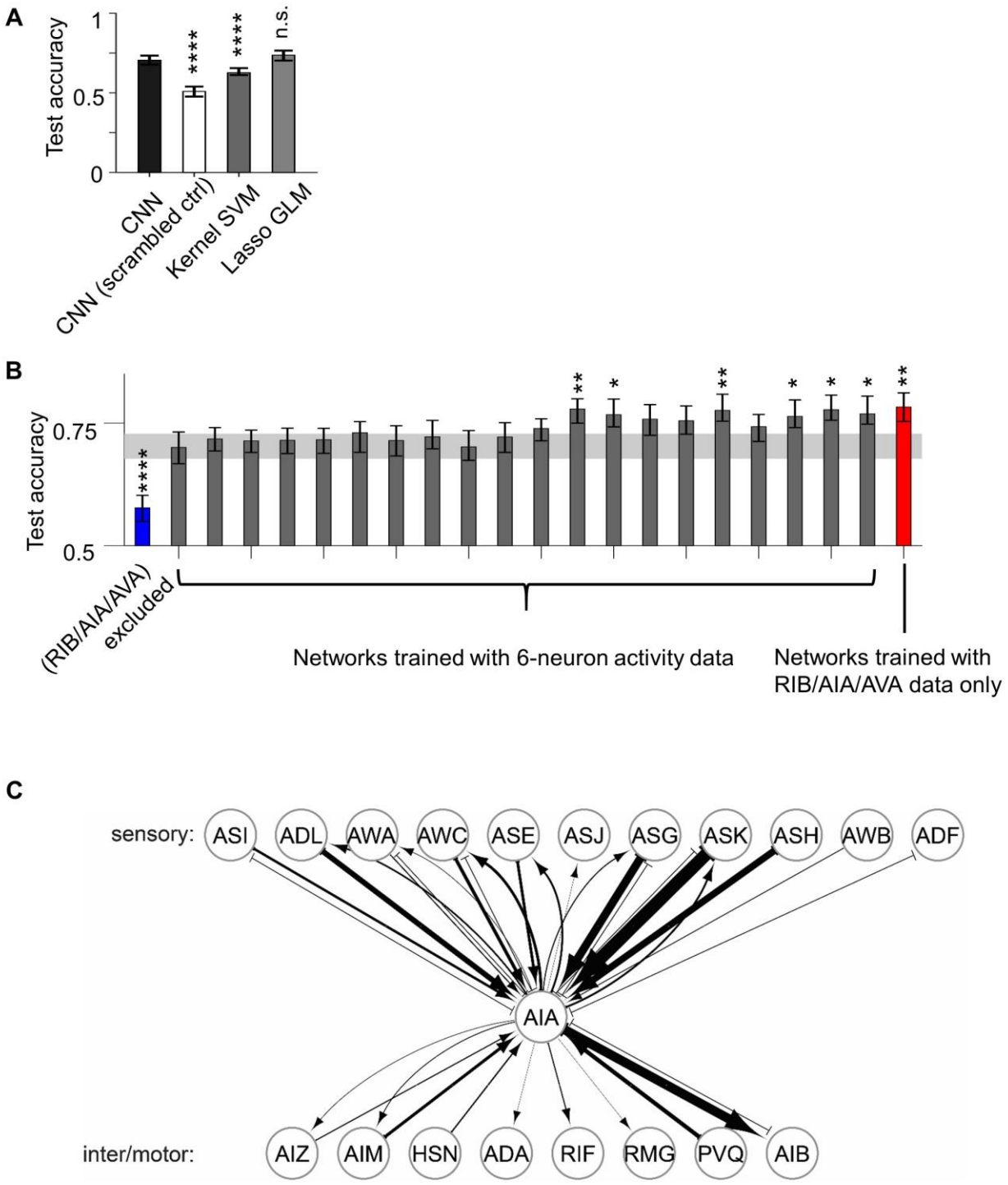
A
Test accuracy
1
0.5
0
****
****
n.s.
CNN
CNN (scrambled ctrl)
Kernel SVM
Lasso GLM
B
Test accuracy
0.75
0.5
****
**
*
**
*
*
*
**
(RIB/AIA/AVA) excluded
Networks trained with 6-neuron activity data
Networks trained with RIB/AIA/AVA data only
C
sensory:
ASI
ADL
AWA
AWC
ASE
ASJ
ASG
ASK
ASH
AWB
ADF
AIA
inter/motor:
AIZ
AIM
HSN
ADA
RIF
RMG
PVQ
AIB

Fig. S4

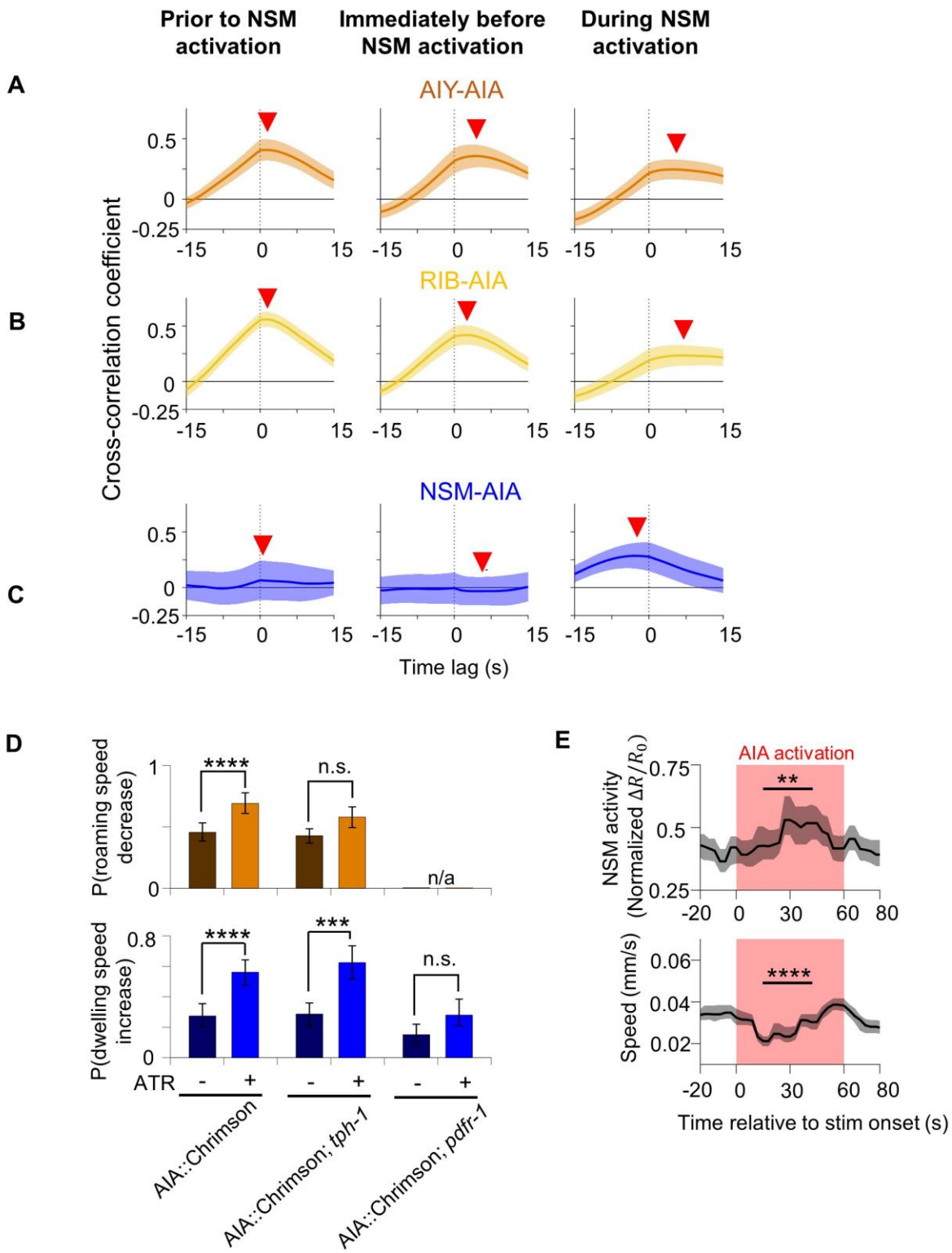
Prior to NSM activation
Immediately before NSM activation
During NSM activation
A
AIY-AIA
B
RIB-AIA
C
NSM-AIA
Cross-correlation coefficient
Time lag (s)
D
P(roaming speed decrease)
P(dwelling speed increase)
****
n.s.
n/a
***
ATR
AIA::Chrimson
AIA::Chrimson; tph-1
AIA::Chrimson; pdfr-1
E
AIA activation
NSM activity (Normalized $\Delta R/R_0$)
Speed (mm/s)
Time relative to stim onset (s)

Fig. S5

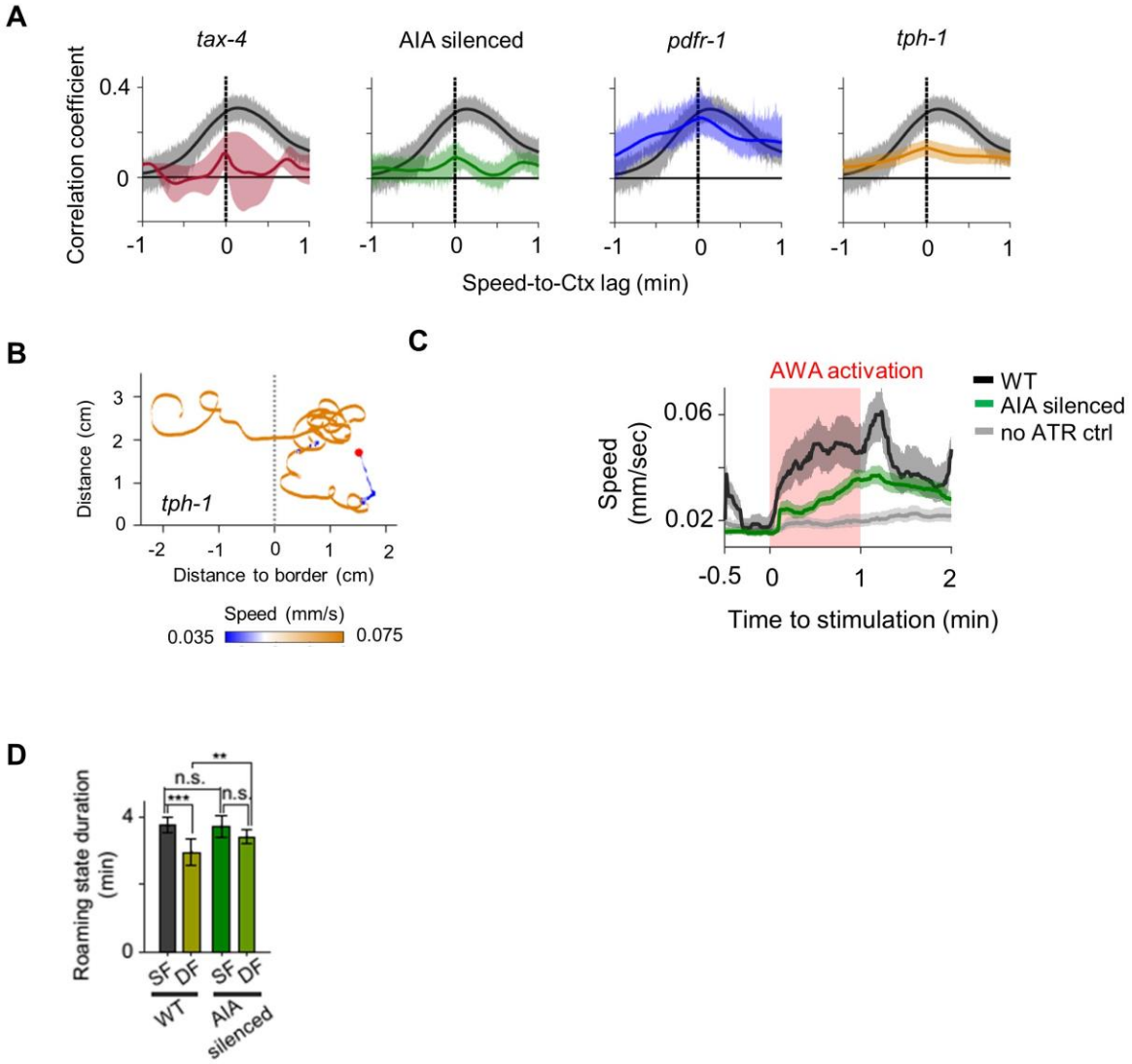
A
tax-4
AIA silenced
pdfr-1
tph-1
Correlation coefficient
0.4
0
-1
0
1
Speed-to-Ctx lag (min)
B
Distance (cm)
3
2
1
0
tph-1
-2
-1
0
1
2
Distance to border (cm)
Speed (mm/s)
0.035
0.075
C
AWA activation
WT
AIA silenced
no ATR ctrl
Speed (mm/sec)
0.06
0.02
-0.5
0
1
2
Time to stimulation (min)
D
Roaming state duration (min)
4
0
n.s.
***
**
n.s.
SF
DF
SF
DF
WT
AIA silenced

Fig. S6

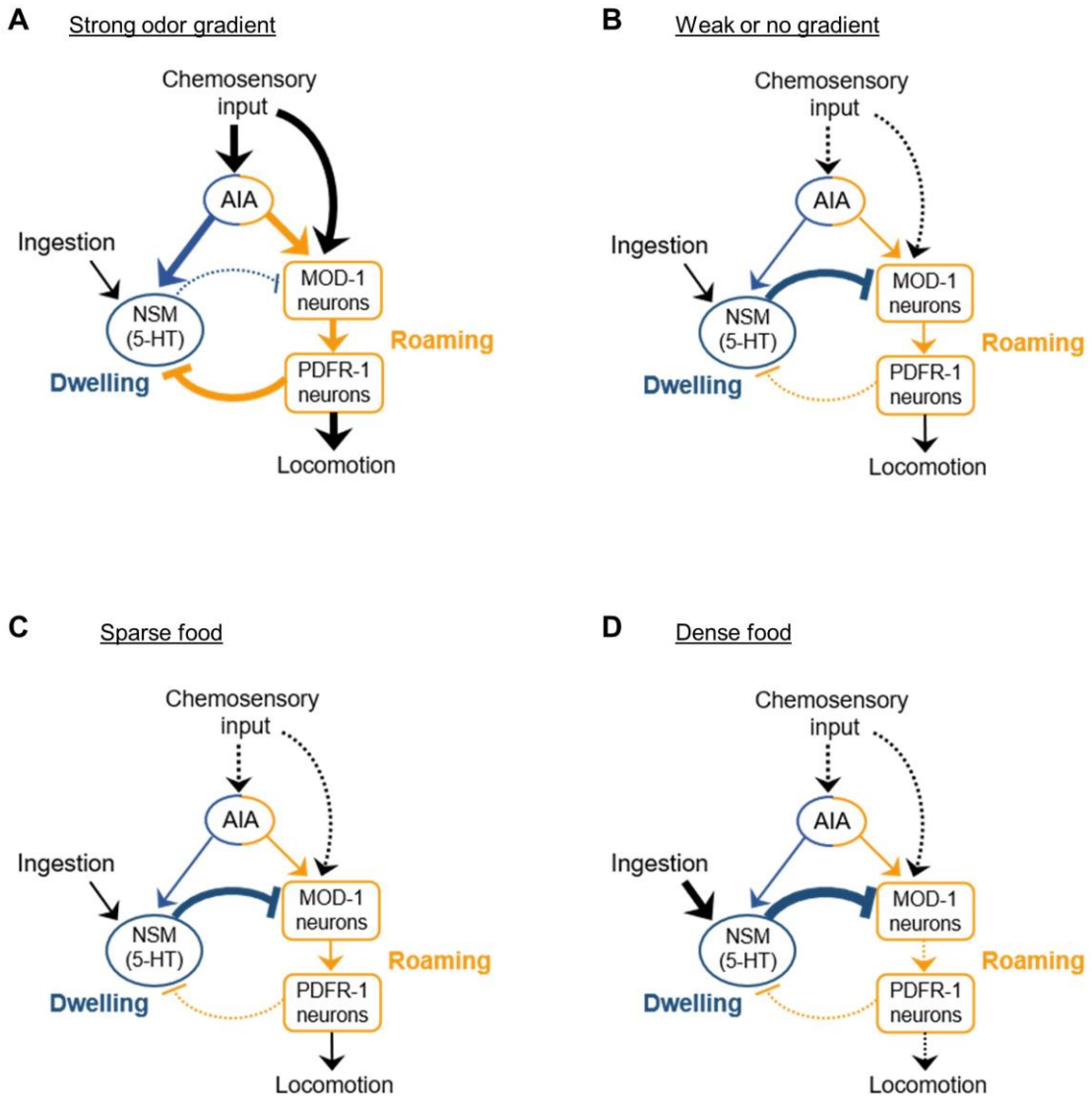
A
Strong odor gradient
Chemosensory input
AIA
Ingestion
MOD-1 neurons
NSM (5-HT)
Roaming
Dwelling
PDFR-1 neurons
Locomotion
B
Weak or no gradient
Chemosensory input
AIA
Ingestion
MOD-1 neurons
NSM (5-HT)
Roaming
Dwelling
PDFR-1 neurons
Locomotion
C
Sparse food
Chemosensory input
AIA
Ingestion
MOD-1 neurons
NSM (5-HT)
Roaming
Dwelling
PDFR-1 neurons
Locomotion
D
Dense food
Chemosensory input
AIA
Ingestion
MOD-1 neurons
NSM (5-HT)
Roaming
Dwelling
PDFR-1 neurons
Locomotion

Fig. S7